Politecnico di Torino

Master’s Degree in Petroleum and Mining Engineering

Depth estimation of subsurface heterogeneity through surface waves attributes

Supervisor:
Laura Valentina Socco

Candidate:
Seyed Amir Afzali Fatatouei

Co-supervisor:
Chiara Colombero

Sessione di Laurea Novembre 2023
A.a. 2023/2024

Acknowledgments

I would like to express my sincere gratitude to my supervisor, Professor Laura Valentina Socco, for her unwavering guidance, invaluable insights, and support throughout my master's degree. Her expertise and encouragement played a pivotal role in my academic career, particularly this research.

I extend my heartfelt appreciation to my co-supervisor, Professor Chiara Colombero, whose mentorship and collaborative spirit significantly contributed to the success of this project. Her thoughtful feedback and dedication to the research are deeply appreciated. She has not only provided me with the necessary technical knowledge but also instilled me her passion and curiosity for geophysics.

I am also immensely thankful to my family for their unwavering support, understanding, and encouragement during this academic journey. Their love and encouragement provided the foundation upon which this achievement stands.

This work is a culmination of the collective efforts of these individuals, and I am truly grateful for their contributions to my academic and personal growth.

Abstract

Surface waves (SWs) can carry important information about the near surface. Near surface characterization is important for several shallow and deep applications of seismic investigations for petroleum and mining engineering. For instance, if there are some oil pipes beneath the surface and there is a major leakage, and a polluted area is formed, surface waves can investigate the anomaly and with this interpretation the anomaly can be modeled. For deep investigations, it is also a common practice to apply corrections to the reflection seismic data (known as static corrections) to eliminate the influence of the shallow weathering layers investigating their properties through surface wave methods. These corrections are made using estimates of the velocity models near the Earth's surface. In addition to the estimation of a velocity model, there are simple effective attributes of SWs that can be used for the identification and location of lateral variations in the subsurface. While their effectiveness in identifying and locating the anomalies has been proven in different studies, the relationship between the anomalies seen in the attribute results and the depth of the detected heterogeneities is still an open scientific question. Between the possible SW attributes, the autospectrum is an effective way to reveal and image the energy content of a seismogram as a function of the frequency content. In this study, the relationship between the frequency band affected by autospectral anomalies and the depth of the heterogeneity is analyzed by means of several numerical models. Three different picking approaches are applied to identify salient frequencies characterizing the anomalies in the autospectra. The selected frequencies are then utilized as inputs in the synthetic model dispersion curves to retrieve the Rayleigh wave velocity value associated with them. With velocity and frequency in hand, the wavelength can be calculated. Several wavelength-depth relationships coming from the literature are then tested and compared to see if they are applicable to the problem. Leveraging the wavelength-depth relationship, the obtained wavelength from the dispersion curve is converted into depth, allowing for the evaluation of the estimation's validity. The ultimate goal of this research is to establish a singular relationship between wavelength and the depth of near surface anomalies with both lateral and vertical heterogeneity. It's important to note that the maximum depth investigated in this work does not exceed 10 meters.

Table of Contents

List of Figures

List of Tables

Chapter 1 Introduction

1.1 Surface wave methods, attributes and related researches

In the field of oil and gas exploration, even though the primary objective is to obtain detailed subsurface imaging, it is crucial to first reconstruct models of the velocity near the Earth's surface. This is because the seismic signals recorded at the surface are captured in the time domain. When seismic waves travel through layers of varying low velocities, especially in the shallow subsurface or onshore areas, these layers, often referred to as weathering layers, can significantly distort the data by masking the reflections from deeper structures. The surface waves mostly are treated as noises, because they can mask the reflected waves and their depth of investigation is very low. The vertical part of surface waves that exhibit low frequency, high amplitude, and a slow group velocity is identified as ground roll. (Yilmaz et al. 1987). The majority of the ground roll in seismic data is made up of surface waves. Traditionally, surface waves (SWs) present in seismic records have been treated as unwanted noise and filtered out during reflection seismic processing. On the other hand, surface waves can carry important information about near surface.

Seismic attributes are measurable or computed elements of seismic data, such as amplitude, that reveal important details about subsurface geological anomalies, like the types of rocks, fluid content, and structural characteristics or heterogeneities. These characteristics are obtained from seismic data by applying different methods of data processing and analysis. In the fields of geophysics and exploration, seismic attributes are used to increase the accuracy of geological and geophysical models as well as the interpretation of subsurface conditions.

The surface wave method (SWM) is a seismic technique that utilizes the analysis of the geometric dispersion of surface waves to characterize subsurface conditions. By examining the dispersion characteristics obtained from seismic recordings, it is possible to invert the data and obtain a local profile of shear wave velocity. In surface-wave (SW) prospecting, significant lateral and/or vertical changes in the near surface can either be a target of investigation or a problem for the reconstruction of trustworthy subsurface models. Colombero et al. (2020) defined four surface wave attributes and tested them for the detection and localization of sharp lateral variations in the shallow subsurface. Energy, energy decay exponent, attenuation coefficient, and autospectrum are some attributes that were used for heterogeneity identification and/or localization.

The autospectral density is a function that displays the energy content of a seismogram. It is a function of both frequency and offset. Colombero et al. (2020) revised and optimized all four attribute approaches for multifold data, and then applied the method to both synthetic and real data. The multifold upgrade enhanced the readability and interpretation of the results by stacking the computed parameters obtained for single-shot or single-offset records. On a wide range of 2D synthetic models that simulate various target geometries, embedding situations, and impedance contrasts with the background, detection and localization abilities are thoroughly assessed. A shallow low-velocity body in a sedimentary sequence and a hard-rock site with two embedded subvertical open fractures were used as two field case studies to evaluate the methodology. To create standard criteria for location estimation, the horizontal gradients of the four parameters were are examined for a quantitative comparison. With errors often comparable to or lower than the geophone spacing, all approaches demonstrate the capacity to detect and locate lateral variations with lower acoustic impedance than the surrounding material.

1.2 Thesis objectives

Subsurface heterogeneities with significant variations in mechanical and physical characteristics may be seen in near-surface seismic surveys. Objects with a lower acoustic impedance than the background are examples of typical heterogeneities. These consist of embedded low-velocity bodies, buried slopes, fractures, and faults. As in the case of steeply dipping mineralized veins and seams or buried ore deposits, variations with higher acoustic impedance than the enclosing medium may also be of interest in other investigations (Colombero et al. 2020). These heterogeneities have the potential to impact a wide range of research outcomes, including geotechnical engineering studies (Hévin et al. 1998; Gischig et al. 2015), potential hydrogeologic and mineral explorations (Bièvre et al. 2012), and regional and local geology (Carpentier et al. 2012; Hyslop and Stewart, 2015; Ikeda and Tsuji, 2016). Due to limitations in ray coverage and refracted ray behavior, ray-based P-wave and S-wave tomography may not be able to adequately identify the location and depth of these sharp variations with desirable detail, especially when facing low-velocity heterogeneities (Colombero et al. 2016; Ikeda and Tsuji, 2016). As opposed to this, surface waves (SWs) that propagate parallel to the ground and attenuate less than body waves can be useful for identifying and capturing images of local heterogeneities. For the purpose of processing SW data, it is also crucial to identify vertical heterogeneities. Some techniques are indeed aimed at the reconstruction of local subsurface 1-D velocity models by assuming a single ratio of wavelength to the depth of the desired anomaly. However, in the presence of lateral variation, this assumption results in inaccurate velocity models.

In this thesis, the theoretical foundation regarding seismic surface waves is first discussed in Chapter 2. The definition of autospectrum and its applicability to heterogeneity localization are addressed. After body waves definitions and their propagation properties, surface waves, their differences with body waves, and their dispersive characteristics are discussed. By knowing surface wave properties, dispersion curves are introduced. Attributes, the definition of autospectrum as an attribute, and its applicability to heterogeneity localization are addressed. As the final goal of the thesis is depth estimation, wavelength is calculated by the autospectrum, and a relationship between wavelength and depth is introduced to examine the autospectrum depth.

In Chapter 3, the numerical models and the results are represented. First, the autospectra of various synthetic models are computed. In the synthetic data, different anomalies with a variety of characteristics are defined as boxes and then the results coming from different approaches of frequency picking are discussed to estimate the depth, several types of frequency picking are defined, so different representative frequencies are retrieved from each autospectrum. These extracted frequencies are used as inputs of the relevant dispersion curve of the model to calculate the wavelength. Wavelength-depth relationships available in the literature are then applied to the results to investigate their applicability for the estimation of the depth of autospectral anomalies. Finally, new wavelength-depth relationships are defined on the obtained numerical results, to improve the estimation.

Chapter 2 Method

2.1 Seismic waves-Difference between body and surface waves

The energy of seismic waves is transported through or along the surface of a medium and causes periodic vibrating vibrations. Body waves and surface waves which are two kinds of waves, are divided into these two categories based on their properties and propagation characteristics. Body waves propagate in all directions from the source and thus travel through the interior of the Earth and surface waves travel along to the interfaces (Evans and Dragoset, 1997).

Body waves are divided into two different types. P-waves, also known as compressional waves, are elastic waves in which the motion of the particles is in the direction of the wave's propagation. Since the P-wave is the fastest seismic wave, it is the first one to arrive at a seismic receiver. It spreads throughout the Earth's solid and liquid layers. Figure 2.1 depicts the P-wave's direction of propagation and direction of vibration. The second kind of body waves is the S-wave. As depicted in Figure 2.2, S- or shear waves are elastic waves in which particles oscillate perpendicular to the direction of the wave's propagation. S-waves have lower propagation velocities than P-waves and can only move through solids because fluids don't experience shear stress. Depending on the direction of oscillation there can be two different kinds of S-wave, which are horizontal S-wave and vertical S-wave shown by S_h and S_v respectively.

S and P waves are the only waves that propagate in a homogeneous infinite medium in all directions. But if there are interfaces other kinds of waves can be produced and propagated which are called surface waves. Surface waves are limited and travel parallel to the interface between the two media. (Sheriff et al. 1990).

Surface waves and body waves are fundamentally different in terms of frequency content, polarization, dispersion, and propagation velocity. Nevertheless, in real cases, surface waves can display highly complex behavior: (1) surface-wave scattering can occur due to near-surface heterogeneities, and a significant portion of the energy may have an incidence out of the receiver-source plane; and (2) surface waves involve modes other than a pure Rayleigh wave that arises when the medium is not homogeneous (Sheriff, 2002).

One of the most important types of surface waves that is applicable to exploration is the Rayleigh wave. It propagates parallel to the surface of the Earth and its amplitude exponentially decreases with depth and this reduction is proportional to the wavelength. In this kind of propagation, the motion of particles is limited to a vertical plane which contains the direction of propagation and they pass through an elliptical route. Retrograde is the name of elliptical particles' motion. The velocity of the Rayleigh wave varies with the wavelength of the wave, as the elastic modulus change with depth. The velocity of the wave is related to the frequency or wavelength and this phenomenon is called dispersion which will be explained in depth later. In Figure 2.3 the propagation of Rayleigh wave is depicted (Sheriff et al. 1990).

The other type of surface wave is Love wave which may be generated between two interfaces. They sometimes are called horizontal S-waves, as they propagate parallel to the surface of the medium. The velocity of the Love wave is higher than the velocity of the S-wave at the surface and lower than the velocity of the S-wave at the layer below. These waves do not have a vast amount of applications in exploration (Sheriff et al. 1990). Other types of surface waves are tube, Stoneley and channel waves.

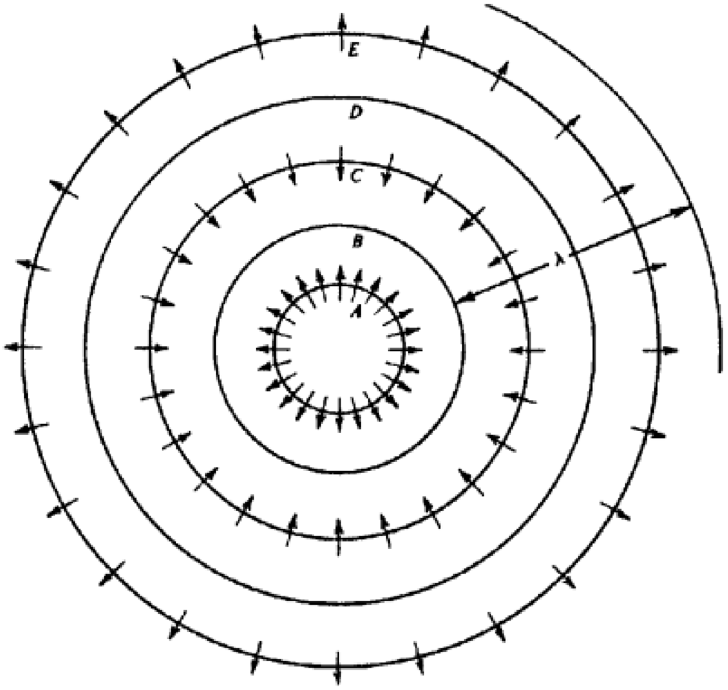

Figure 2.1 Displacement for a spherical P-wave (Sheriff et al. 1990)

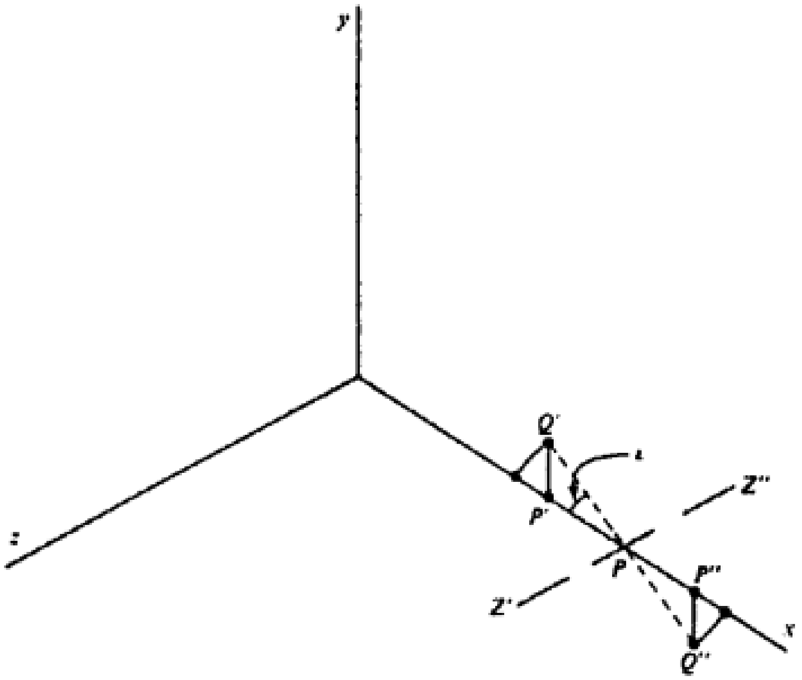

Figure 2.2 Motion during S-wave propagation (Sheriff et al. 1990)

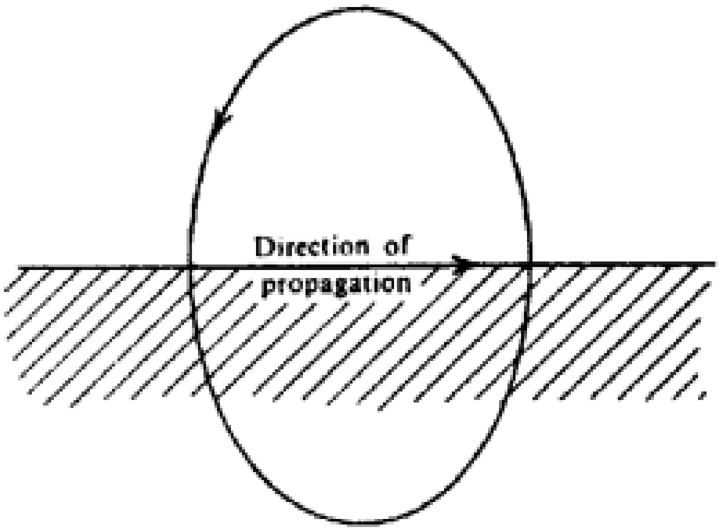

Figure 2.3 Movement of particle due to Rayleigh wave propagation

2.2 Dispersion of surface waves

Dispersion, as it is described in Section 2.1, is the dependency of the velocity of the surface waves on frequency or wavelength. Dispersion occurs when waves of different frequencies travel at different velocities. All the applications of surface waves explained in the first chapter exploit the propagation velocity of surface waves as a function of frequency (D. Boiero, L.V. Socco, 2011). A dispersion curve is therefore a graphical representation that depicts how the phase velocity of seismic waves varies with frequency or wavelength. In other words, dispersion curves illustrate the connection between phase velocity and frequency. Seismic records often contain surface waves (SWs), which can be analyzed to extract local dispersion curves (DCs) and their characteristics are influenced by the velocity model in the propagation path (Strobbia et al. 2011). As illustrated in Figure 2.4 low frequencies with long wavelengths enter high-depth layers, while high frequencies with short wavelengths travel near the surface.

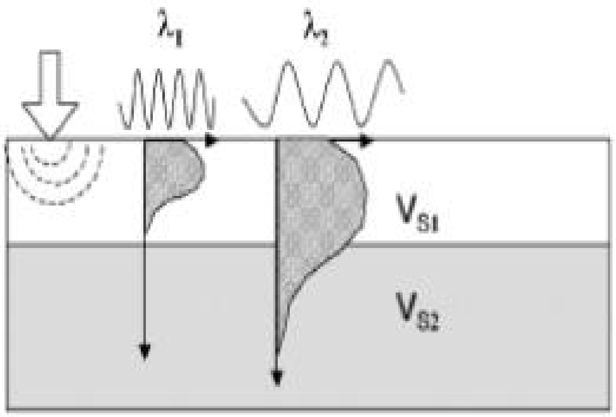

Figure 2.4 Depicted the dispersion of Rayleigh wave. λ_1 related to the wave traveling in a homogeneous medium, while λ_2 related to the wave which travels in a vertically heterogeneous medium (Socco and Strobbia, 2004).

2.3 S-wave and P-wave velocity models from SW analysis

A local 1D velocity model can be produced by inverting the DC, if each DC corresponds with a small subsurface area (Socco et al. 2017). These curves are an essential tool for identifying how seismic waves appear in different mediums and for analyzing the Earth's subsurface structure. These DCs provide valuable information for estimating S-wave velocity models in the near-surface region. The direct determination of one-way time is facilitated by the time-average velocity, which is obtained by considering a reference datum plan depth. This method relies on having a 1D S-wave velocity model and the corresponding dispersion curve for the seismic line.

As it is said already, in order to estimate the dispersion curves of surface waves, it is common practice to suppose that they propagate via a 1D medium; however, lateral changes along the propagation path might play a significant role that merits special consideration. As demonstrated by Kennett and Yoshizawa (2002) and Strobbia and Foti (2006), a wave path with horizontal heterogeneity can affect the measured phase velocity of the surface waves. The inversion used to get S-wave velocity models is therefore affected by the lateral variations (Lin and Lin 2007). A seismic line is frequently used to obtain a number of dispersion curves, which are then inverted under the assumption of 1D models. A 2D/3D final V_s distribution is produced by combining the results or interpolating them (Grandjean and Bitri 2006). Thus, the impact of lateral variations on each dispersion curve is disregarded, and the resulting V_s model is taken to be a good representation of the site with smooth fluctuations. Depending on the type of lateral variations present and the processing method employed, the above assumption may not always hold true.

Based on the research by Boiero and Socco (2011), through some calculations, a wave field is retrieved. By using any wave field transformation like f-k, dispersion curves can be obtained in a 1D environment without lateral variation. The frequency and slowness (or wavenumber) are calculated in a domain and the corresponding energy is shown in order to picture the dispersive waves. The propagation of surface waves is realized by having the high amplitude of surface waves and through the recognition of frequency and velocity. As it is illustrated in these researches all of them are ignoring the lateral variation and they suppose lateral homogeneous models. In this study, the aim is to estimate the depth of an anomaly with lateral variation.

It is shown that the dependency of surface waves dispersion on the velocity of the P-wave is negligible, so we can obtain the Poisson's ratio from other calculations and use it with the combination of the S-wave velocity model to estimate the P-wave velocity model by using the Equation 2.1(Socco and Comina 2011).

$$v = \frac{\left(\frac{Vp}{Vs}\right)^2 - 2}{2\left(\frac{Vp}{Vs}\right)^2 - 1} \tag{2.1}$$

Where Vp is the velocity of P-wave, Vs is the velocity of S-wave and ν is the Poisson's ratio. Socco and Comina (2011) showed that the surface waves cannot be used to estimate a velocity model without utilizing other independent data. From Figure 2.4 where the plot of the Equation 2.1 is depicted, it is obvious that the dependency of V_p/ V_s in different ranges of Poisson's ratio differs.

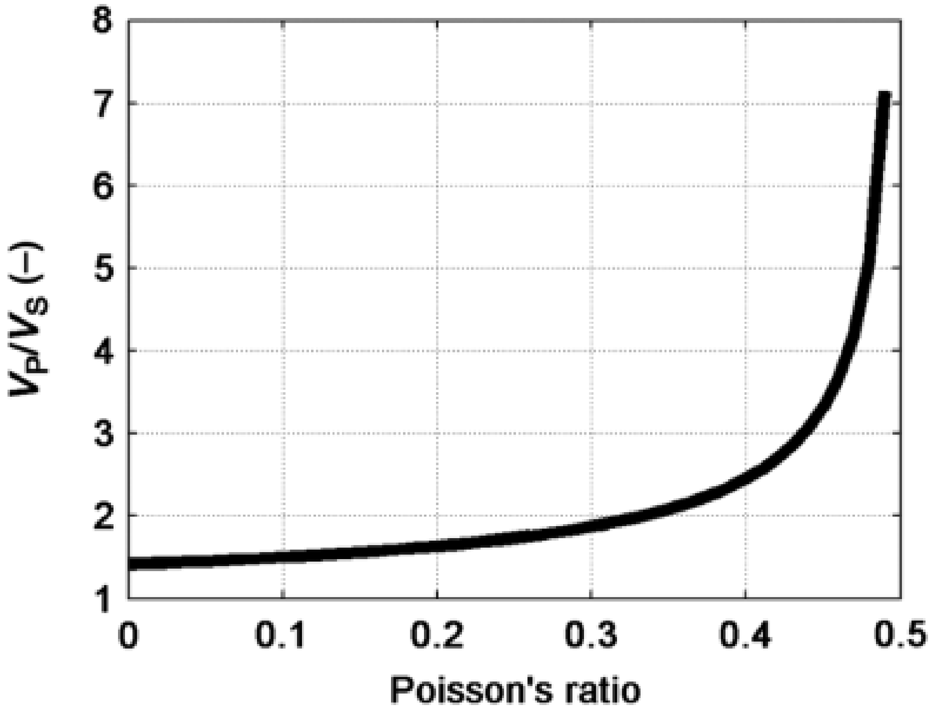

Figure 2.5 Equation 2: Poisson's ratio versus Vp/Vs

There is wide recognition in the scientific literature regarding the potential of analyzing SWs to extract near-surface S-wave velocity models (Haney and Miller, 2013). The phase velocity of Rayleigh waves is close to the velocity of the shear wave in sediments (Pierre-Yves Bard 1985). For static computation, near-surface velocity models can be estimated using analysis of surface waves. In recent times, also rough methods for estimating statics from dispersion curves of surface waves without the need for an inversion algorithm have been proposed and they are still applicable to retrieve the desired velocity model (Socco, Mabyalaht 2015).

Socco et al. (2017), showed that to estimate near-surface S-wave velocity models, local dispersion curves (DCs) can be extracted from seismic data that contain surface waves (SWs). The authors concentrated on directly inverting the data and estimating time-average S-wave velocity models from SW DCs. By using a datum plan depth and time-average velocity, one may easily calculate one-way time. In this method by knowing the one-dimensional shear wave velocity model of a seismic line and its related dispersion curves, the relationship between investigation depth and surface wave wavelength can be estimated. The other time-average S-wave velocity models along the line are then estimated directly from the DCs using a data transformation and this wavelength-depth relationship. This solution eliminates the need for substantial data inversion and offers a straightforward process appropriate for industrial processes. The technique was tested on synthetic and real data of real acquisition, and the time-average velocity models showed less than 10% error at locations with lateral velocity variations.

The method can be extended to the retrieval of a P-wave velocity model (Socco et al. 2017). As well as for the S-wave models, a W-D relationship is estimated from surface waves using an established one-dimensional shear wave velocity model along the line and its corresponding dispersion curve. The Poisson's ratio affects the W-D relationship, thus a straightforward approach for calculating an "apparent" Poisson's ratio profile is then created, which is the Poisson's ratio value that connects the velocity of the S-wave to the velocity of the P-wave. In order to create time-average velocity models of P-wave, the velocity models of S-wave calculated from the dispersion curves are converted. Again on both synthetic and real-world data, the method is evaluated, and they discovered that it is capable of obtaining P-wave velocity models with less than 10 percent uncertainty in laterally heterogeneous sites.

2.4 Surface wave attributes

Surface wave attributes are measurable or computed characteristics derived from the analysis of surface waves in seismic explorations. Attributes provide valuable information about subsurface properties and can be used for various applications such as the kinds of rocks present, their fluid content, and any structural heterogeneities or features. For instance, the phase velocity of surface waves is an essential attribute. It is the speed at which a specific wave phase propagates. Variations in phase velocity can indicate changes in subsurface properties. The frequency content of surface waves can provide insights into the subsurface structure. Different frequencies may interact with subsurface materials in unique ways, allowing for structural identification. The amplitude of surface waves can reveal information about the subsurface's attenuation properties. Attenuation is a measure of how quickly seismic energy is absorbed and dispersed.

Numerous seismic attributes have been proposed in recent decades to identify, describe, and filter surface waves. Determining which of these attributes is more appropriate in a given situation or even whether they are independent is a challenging task (Galvis et al. 2017).

Finding the energy of the seismic traces obtained along a profile is one of the most straightforward methods to localize sharp lateral variations. The energy of a receiver is a function of amplitude at each frequency and offset. In the presence of back reflection or energy trapping, energy concentration or decay is expected. Colombero et al. (2017) by using this method located open fractures within a granitic rock mass Back reflection at the discontinuity interfaces were considered to be the cause of energy concentrations at fracture locations.

The energy decay exponent is the negative power that relates the distance ratio of two adjacent receivers to their energy proportion. If there is no lateral heterogeneity, by disregarding the intrinsic attenuation and recovering the geometrical spreading, the energy decay exponent is expected to be zero. In the case of energy decay, it is positive, while concentration causes a negative energy decay exponent due to back reflection and/or energy trapping in the heterogeneity.

This observation is in coherence with the previous attribute results. This method was adopted for multifold data by Socco and Bergamo (2014).

Sharp lateral variations can be identified and located with the use of the evaluation of marked and localized changes in seismic wave attenuation in the subsurface. By disregarding the geometrical spreading the attenuation coefficient at each frequency is a function of the energy of two subsequent receivers and their offset. The local attenuation of various frequency components of the propagating wave field is measured by the attenuation coefficient. When a sharp lateral variation is observed, energy reflection at the interface has a significant impact on the attenuation. So this attribute can be used for the localization of heterogeneity.

2.4.1 Autospectrum

Zerwer et al. (2005) initially convinced the autospectrum method for the identification of cracks in concrete beams. The autospectral density of a signal shows the energy content distribution throughout a defined frequency range. The autospectral density (G_{xx}) of a seismic trace z(t) is determined by summing the squared real and imaginary components of the discrete Fourier transform Z(w) of each trace, as following:

$$|G_{xx}|=\{Re[Z(w)]\}^2+\{Im[Z(w)]\}^2 \tag{2.3}$$

As a result, calculating G_{xx} for a common-shot gather offers an approach to represent the energy distribution of a seismogram based on frequency and offset.

As an example in Figure 2.6, exemplificative autospectra computed on a synthetic model, described in the following, are shown. The model consists of a homogeneous material with a box-shaped anomaly with the length of 7 m in the center of the seismic line. The acoustic impedance at the interface between the box and the background material is -0.48. The four autospectra are related to four different modeled depths of the box anomaly (from 2 m to 8 m).

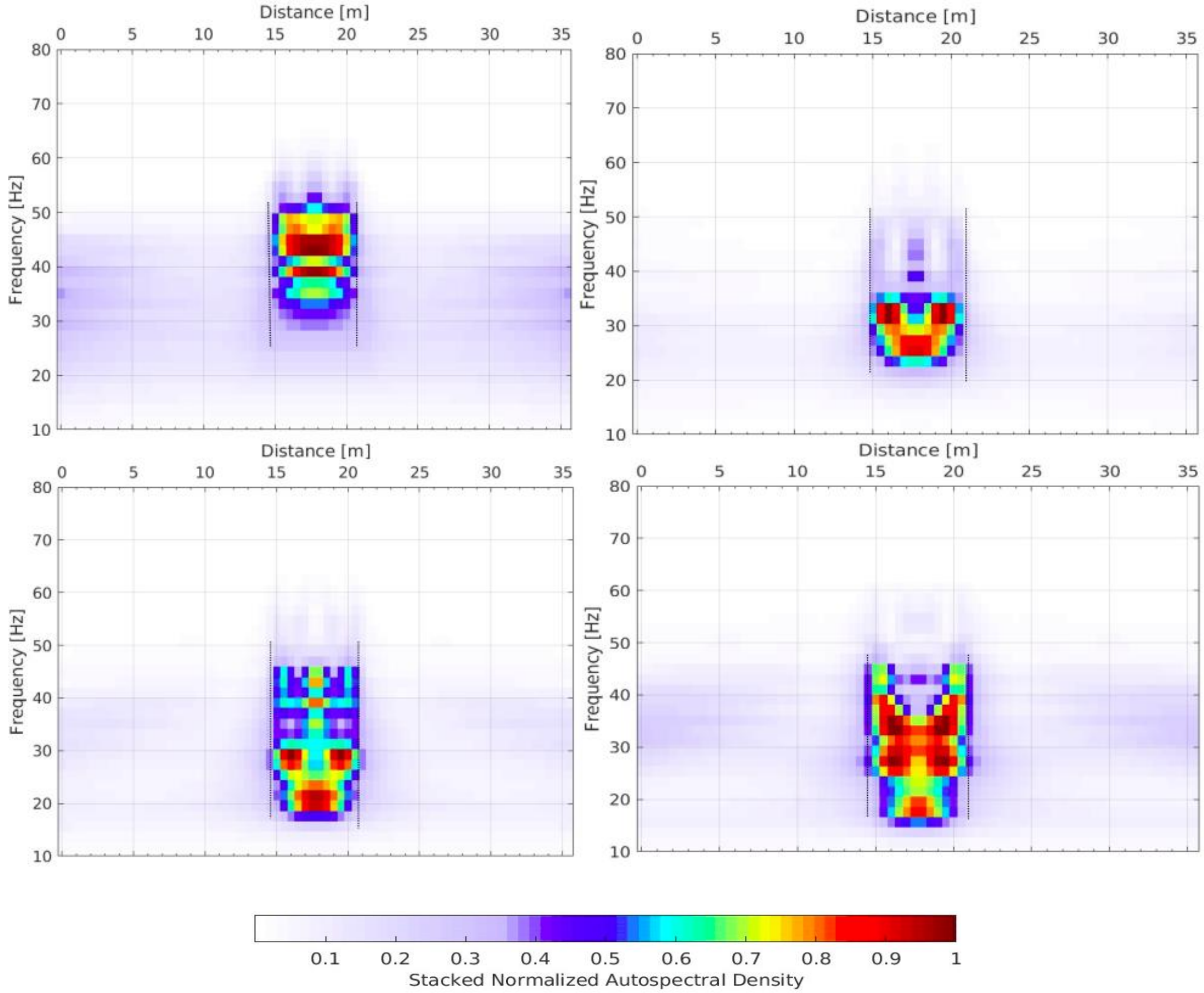

Figure 2.6 Autospectra of Box 1 for different depths. Autospectrum of anomalies with 2 m (top left), 4 m (top right), 6 m (bottom left) and 8 m (bottom right) depth. The lateral limits are shown by dashed lines.

All the model parameters are constant, with the only exception of the box depth. Varying the depth of the box, the frequencies that are affected by the high-energy anomaly change in each autospectrum. As an example, increasing the depth of the box, the frequency is decreasing at the lower boundary of the autospectral anomaly.

The aim of this research is to investigate the relationship between the depth of the anomaly and the affected frequencies (or wavelengths). In other words, the final goal is the estimation of the depth of the box through the fast autospectral computation.

2.4.2 Depth estimation from surface wave attributes

The estimation of depth from SW attributes is a challenging subject. Different authors proposed different relationships between the frequency or wavelength interested by the anomaly in the attribute plots and the depth of the target. These wavelength-depth relationships are summarized in Table 2.1. Depending on the attribute, the wavelength λ is usually divided by an integer number to retrieve a rough estimation of the maximum depth z of the anomaly, following:

$$Z=\lambda/K \tag{2.4}$$

Where k is a constant integer value, varying from 1 to 3, depending on the authors.

Table 2.1 The relationships between wavelength and depth in different researches to retrieve 1-D velocity model

Authors	Method	Data	Depth
Hévin et al. (1998)	T/I Spectral Ratios	Synthetic (cracks in concrete)	λ/3
Shtivelman (2003)	Power spectrum	Synthetic (void in layered model)	λ/2
Zerwer et al. (2005)	Autospectrum	Real (cracks in concrete)	λ
Nasseri-Moghaddam et al. (2005)	NALD	Synthetic (void detection)	λ
Bièvre et al. (2012)	T/I Spectral Ratios	Real (fractures in clay landslide)	λ/3
Bergamo and Socco (2014)	Autospectrum	Synthetic and real (fault zone)	λ
Hyslop and Stewart (2015)	Reflectivity	Synthetic and real (fault zone)	λ/2
Ikeda and Tsuji (2016)	Attenuation Coefficient	Synthetic and real (fractures and faults)	λ/3

Wavelength-depth relationships are also described in the literature for the direct transformation of dispersion curves, without the need for extensive inversion schemes. These relationships seem suitable for the retrieval of velocity models, but they've never been tested on the SW attributes.

Surface waves propagate over the free surface across a cylinder whose thickness varies on the wavelength. Due to this property, surface waves in a heterogeneous media in the vertical direction, reveal their dispersive behavior. Depending on the S-wave velocity of the layers from the surface until the wave front thickness, the velocity of propagation related to each wavelength will vary. Calculating the displacements triggered by the surface wave propagation at various depths can demonstrate this (Socco et al. 2017).

When there are a lot of dispersion curves that should be inverted it is not a smart way to do it one by one. The time-average velocity at the depth of the datum plan must be precise enough to show the lateral variability of the static displacement along the line in order to estimate the static corrections. Equation 2.2 illustrates at a certain depth (h), the time average velocity (Vz):

$$V_z = \frac{\sum_n h_i}{\sum_n \left(\frac{h_i}{V_i}\right)} \tag{2.2}$$

Where h is the depth, h_i and V_i are the thickness and the velocity of the *i*th layer respectively and n is the number of layers until that depth. Also Socco et al. (2017) referred the time-average S-wave velocity as V_{sz}. In the area of seismic hazard studies, Brown et al. (2000), Comina et al. (2011), and Aung and Leong (2015) focused on the reliability of V_{sz} estimation. Since this parameter is used to categorize sites for seismic zonation, they worked on the estimation of the V_{sz} at 30 m depth. Through the analysis of surface waves, they demonstrated how accurate the estimate of V_{s30} is. Furthermore, they proved that the value of V_{s30} accurately represents the SW phase velocity at a particular wavelength with a reasonable degree of uncertainty. The above-mentioned relationship implies a strong connection between the phase velocity at a specific wavelength and the V_{sz} at a particular depth. Or to put it another way, there is a relationship between the wavelength and the Z. A weighted average velocity approach, which is based on the influence of the impact made by different layers on the velocity at a particular wavelength, has been the subject of some research (Leong and Aung, 2012). Furthermore, following a data transformation, Socco et al. (2015) developed the idea of the relationship between depth and wavelength, to the calculation of the V_{sz} at any depth. The wavelength of the dispersion curve and the depth of the V_{sz} profile, which corresponds to the point at which the S-wave velocity equals the phase velocity of Rayleigh waves, were found to be linearly related. The dispersion curve can be converted into a V_{sz} model using this relationship, which offers the one-way time value at any depth within the investigation limit. Socco et al. (2017) then used polynomial fitting to enhance the estimation of the wavelength-depth relationship while also examining the uncertainties and the effects of utilizing a particular reference velocity profile in the data. In Figure 2.5 an example in which, a 1D layered velocity model, its V_{sz}, and the dispersion curve as a function of wavelength is shown. The arrows in Figure 2.5.a focus on the above-mentioned status, where the wavelength should be derived for a given V_{sz} by finding an equal value of phase velocity and V_{sz}.. Figure 5.2.b shows pairs of values for wavelength and depth when phase velocity and Vsz are equal, followed by polynomial fitting that makes it possible to extract Vsz from the dispersion curve in the range of the inquiry depth limit as a continuing parameter.

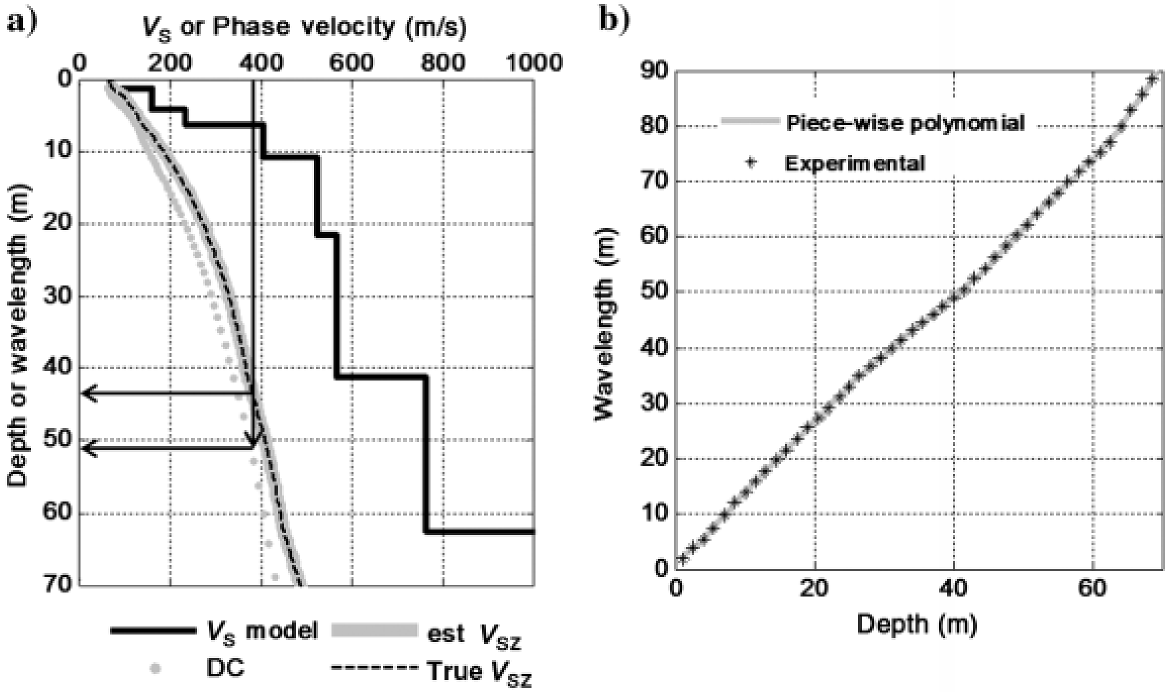

Figure 2.7 (a) Vertical axis related to the depth for S-wave velocity and to wavelength for the DC, while the horizontal axis related to S-wave velocity profile for S-wave velocity and to the SW phase velocity for the DC. The synthetic S-wave model, its corresponding true Vsz, the DC of Rayleigh wave and the estimated Vsz are depicted. (b) The wavelength-depth pairs and the fitting polynomial which the W-D relationship can be retrieved (Socco et al. 2017).

This relationship can be demonstrated by calculating the displacements caused by the propagation of SWs at various depths. The wavelength-depth relationship approximately represents the threshold at which the displacements become insignificant, reaching around 10% of their original magnitude. By establishing a relationship between the wavelength of surface waves and the investigation depth within the time-average velocity model, it becomes possible to estimate the time-average S-wave velocity models at other points along the line directly from the DCs. This approach eliminates the need for complex data inversion processes and offers a straightforward method that is well-suited for industrial workflows. (Socco et al. 2017) The lack of uniqueness in the inversion process is a widely acknowledged disadvantage of surface wave analysis.

The above described method can therefore be potentially suitable for the transformation of the autospectral frequency or wavelength into a depth. To test its applicability, in the present work we extracted some reference frequencies from autospectrum and, then entered the frequency value into the dispersion curve of the model to obtain a wavelength. We then tested the wavelength-depth relationship to determine its validity for the conversion of the autospectrum depths.

Chapter 3 Data, Processing, and Results

3.1 Flowchart

In this chapter, we first give an overview of what is explored in this research by explaining the workflow and showing the flowchart. Then we introduce the numerical models and data, as well as the processing steps that are applied to them, such as autospectrum, dispersion curves, wavelength-depth relationship, and depth estimation. At the end, there will be a comparison between the real depth and the estimated one, also an evaluation of how reliable this approach is.

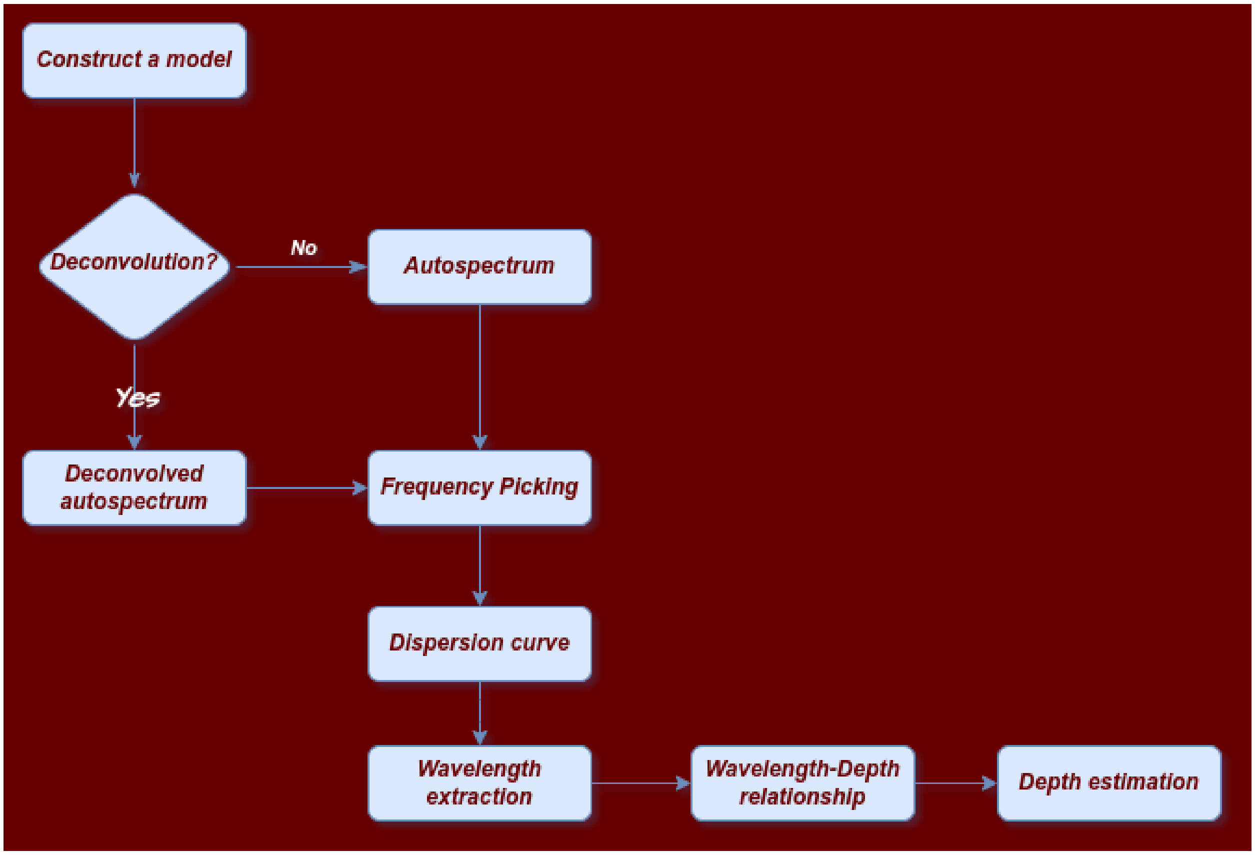

Figure 3.1 The research flowchart

As depicted in Figure 3.1, the proposed workflow is applied to synthetic simulations with different geometry, model parameters, and physical properties. The autospectrum is computed on the raw data of the simulations and on the deconvolved data obtained on the synthetic model. The need for deconvolution is further explained in the following. When the autospectrum is obtained, some reference frequencies are identified in it, i.e. the frequency corresponding to the bottom of the anomaly, the one corresponding to the maximum of the anomaly, and the frequency corresponding to the maximum vertical gradient of the autospectra of the traces acquired on the top of the anomaly. These reference frequencies are converted into wavelengths exploiting the synthetic dispersion curves computed on the top of the box heterogeneity. The wavelength-depth relationships described in Section 2.4.2 are then tested on the results. Since no clear applicability of any of the literature equations seems suitable for the depth estimation, new wavelength-depth relationships are proposed for the depth estimation.

3.2 Numerical model

In order to evaluate the efficacy of our approach, various synthetic models, including a localized heterogeneity that served as the detection target, were developed in COMSOL Multiphysics. Figure 3.2 illustrates the model schematic, which consists of a homogeneous background(Material 1) and a box-shaped target heterogeneity (Material 2), varying in length, depth, and physical parameters such as Poisson's ratio and acoustic impedance contrast with respect to the background, in different models.

As a comparison, a layered model with two layers having the same material properties (Material 2 at the top, Material 1 for the halfspace) is defined. To prevent reflections, a half-space configuration with low reflecting boundaries at the bottom and lateral sides of the domain was adopted for all models, with a height equal to 1000 meters and a width equal to 2000 meters. The bottom corner points were also fixed to have zero displacement. A free surface defines the top boundary.

Figure 3.3 shows a synthetic array of 72 geophones with half-meter spacing that was simulated on the top of the model, for a total length of 35.5 m (from G1 to G72). Seven source positions were located along the seismic line, with a move-up rate of 12 geophones at its endpoints (S1 and S7) and within the array (S2-S6, Figure 3.3). A Ricker wavelet with three different central frequencies was used as seismic input at the different source locations. The central frequencies were 30 Hz, 45 Hz, and 60 Hz. Rayleigh damping was added to the models for all materials in accordance with the Q values shown in Table 3.1.

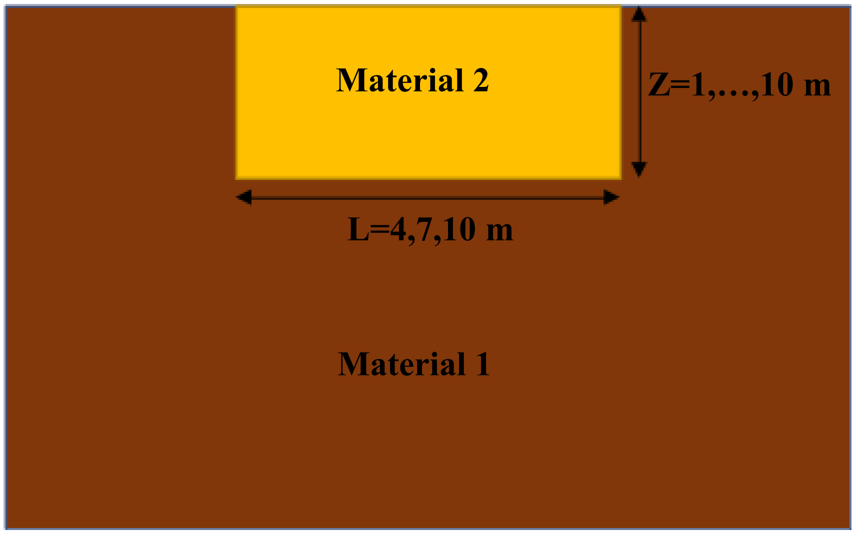

Figure 3.2 Schematic section of the 2D synthetic models.

Table 3.1 Physical and mechanical parameters of the different synthetic models.

		VP [m/s]	VS [m/s]	VR [m/s]	v [-]	ρ [kg/m3]	Z [m]	L [m]	E [Pa]	G [Pa]	Q [-]	eta	f1	f2	alpha	beta	AI	RC
BOX1	MAT2	1040	600	552	0.25	2200	-	-	1.98E+09	7.93E+08	30	0.02	30	70	4.40	5.3E-05	2287981	-
BOX1	MAT1	400	231	212	0.25	2000	1-10	7	2.67E+08	1.07E+08	20	0.03	30	70	6.60	8.0E-05	800050	-0.48
BOX2	MAT2	1001	613	559	0.2	2200	-	-	1.98E+09	8.26E+08	30	0.02	30	70	4.40	5.3E-05	2201611	-
BOX2	MAT1	385	236	215	0.2	2000	1-10	7	2.67E+08	1.11E+08	20	0.03	30	70	6.60	8.0E-05	769848	-0.48
BOX3	MAT2	1102	589	546	0.3	2200	-	-	1.98E+09	7.63E+08	30	0.02	30	70	4.40	5.3E-05	2423311	-
BOX3	MAT1	424	226	210	0.3	2000	1-10	7	2.67E+08	1.03E+08	20	0.03	30	70	6.60	8.0E-05	847372	-0.48
BOX4	MAT2	1040	600	552	0.25	2200	-	-	1.98E+09	7.93E+08	30	0.02	30	70	4.40	5.3E-05	2287981	-
BOX4	MAT1	606	350	322	0.25	2000	1-10	7	6.13E+08	2.45E+08	20	0.03	30	70	6.60	8.0E-05	1212930	-0.31
BOX5	MAT2	1040	600	552	0.25	2200	-	-	1.98E+09	7.93E+08	30	0.02	30	70	4.40	5.3E-05	2287981	-
BOX5	MAT1	814	470	432	0.25	2000	1-10	7	1.11E+09	4.42E+08	20	0.03	30	70	6.60	8.0E-05	1628496	-0.17
BOX6	MAT2	1040	600	552	0.25	2200	-	-	1.98E+09	7.93E+08	30	0.02	30	70	4.40	5.3E-05	2287981	-
BOX6	MAT1	400	231	212	0.25	2000	2,4,6,8,10	4	2.67E+08	1.07E+08	20	0.03	30	70	6.60	8.0E-05	800050	-0.48
BOX7	MAT2	1040	600	552	0.25	2200	-	-	1.98E+09	7.93E+08	30	0.02	30	70	4.40	5.3E-05	2287981	-
BOX7	MAT1	400	231	212	0.25	2000	2,4,6,8,10	10	2.67E+08	1.07E+08	20	0.03	30	70	6.60	8.0E-05	800050	-0.48
LAYERED	MAT2	1040	600	552	0.25	2200	-	-	1.98E+09	7.93E+08	30	0.02	30	70	4.4	5.3E-05	2287981	-
LAYERED	MAT1	400	231	212	0.25	2000	2,4,6,8,10	-	2.67E+08	1.07E+08	20	0.03	30	70	6.6	8.0E-05	800050	-0.48

Starting from the Box 1 configuration, we implemented different models to investigate the impact of various parameters on the autospectrum. Specifically, Box 1, Box 2, and Box 3 differ in the Poisson's ratio of the materials, Box 4 and Box 5 have the same parameters for Material 2, but differences in Material 1. As a consequence, they differ in the contrast in acoustic impedance at the interface between the background and the box. In Box 6 and Box 7, the materials are the same as in Box 1, but the box heterogeneity has variable length. The final model is a layered model consisting of two stacked layers without lateral variation having the material properties of Box 1.

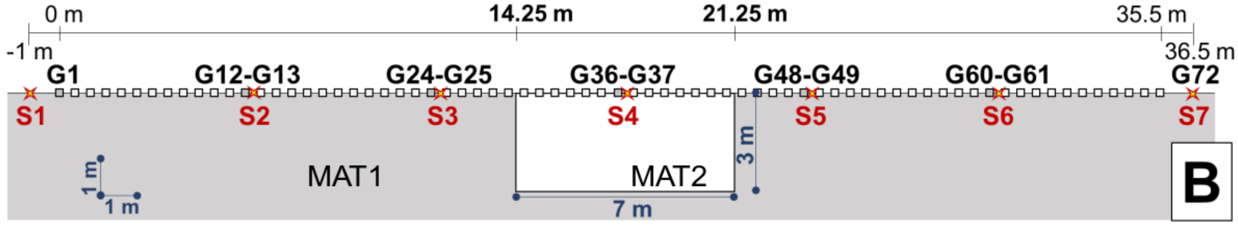

Figure 3.3 Schematic view of the seismic array on one of the synthetic models (Box 1, with depth = 3 m).

3.3 Results of the autospectrum

Although all the results of the research will be considered for final evaluations, only few examples of autospectrum computation from different depths of the box are shown in the following. As it is mentioned all the models configurations were tested for variable depths of the box between 1 to ten m, however only some reference depths are shown in the following figures for clarity. As an example, Figure 3.4 shows the autospectra computed with Box1 model configuration and a 30-Hz Ricker wavelet, for depths of the box from 2 to 10 m. Analyzing the results, it is clear that the anomaly depicted in the autospectra is shifted to lower frequencies while increasing the thickness of the box.

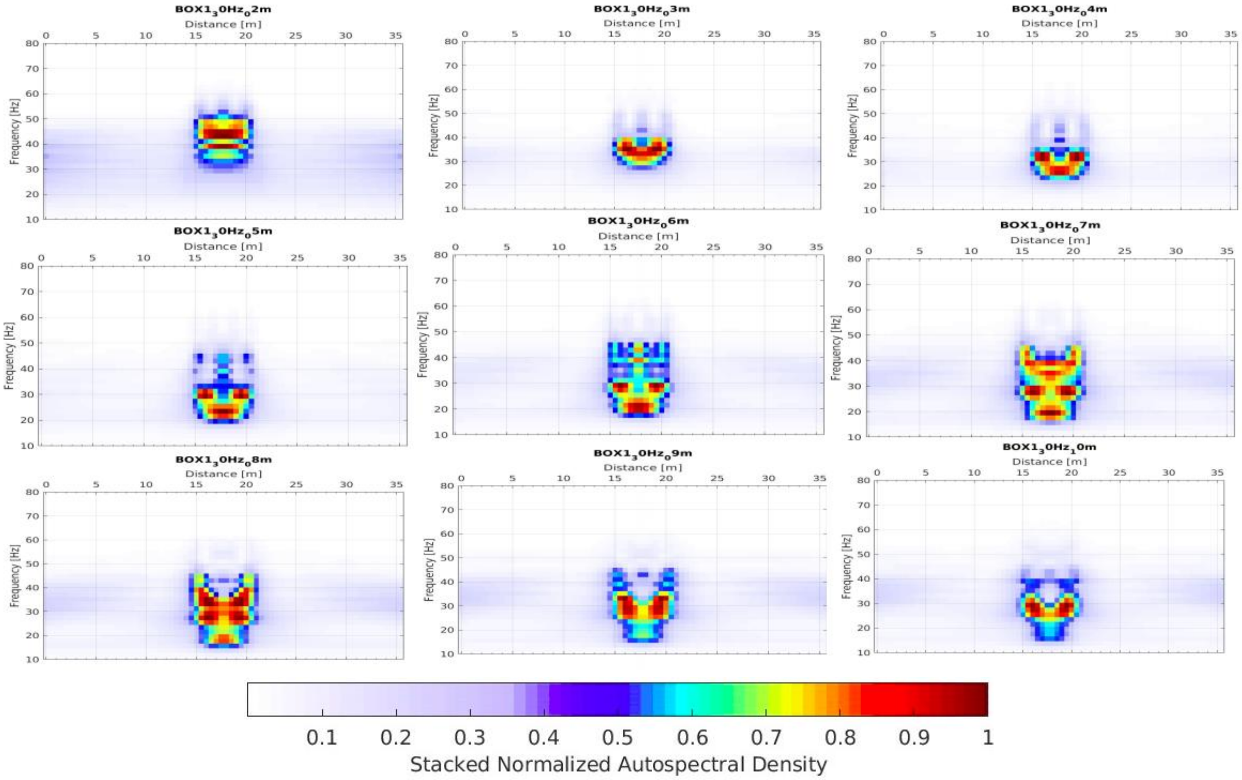

Figure 3.4 Autospectra of Box 1 computed on the simulations that adopted Ricker wavelet with central frequency equal to 30 Hz, lateral length equals to 7 m and depth from 2 m to 10 m.

3.3.1 Source effect

In order to investigate the probable impact of the central frequency of the wavelet of the source, Box 1 was modeled with three different central frequencies, which are 30 Hz, 45 Hz, and 60 Hz. Figures 3.5, 3.6, and 3.7 illustrate the autospectrum computed on Box 1, with the central frequencies of the wavelet equal to 30 Hz, 45 Hz, and 60 Hz respectively. The most obvious trend that can be retrieved from these autospectra is that with increasing depth, the minimum frequency in the autospectrum is decreasing, as already depicted in Figure 3.4. This trend illustrates that there could be a meaningful relationship between the depth of the anomaly and the frequency. However, the frequency band interested by the anomaly is sensibly different if a different source is applied to the same model.

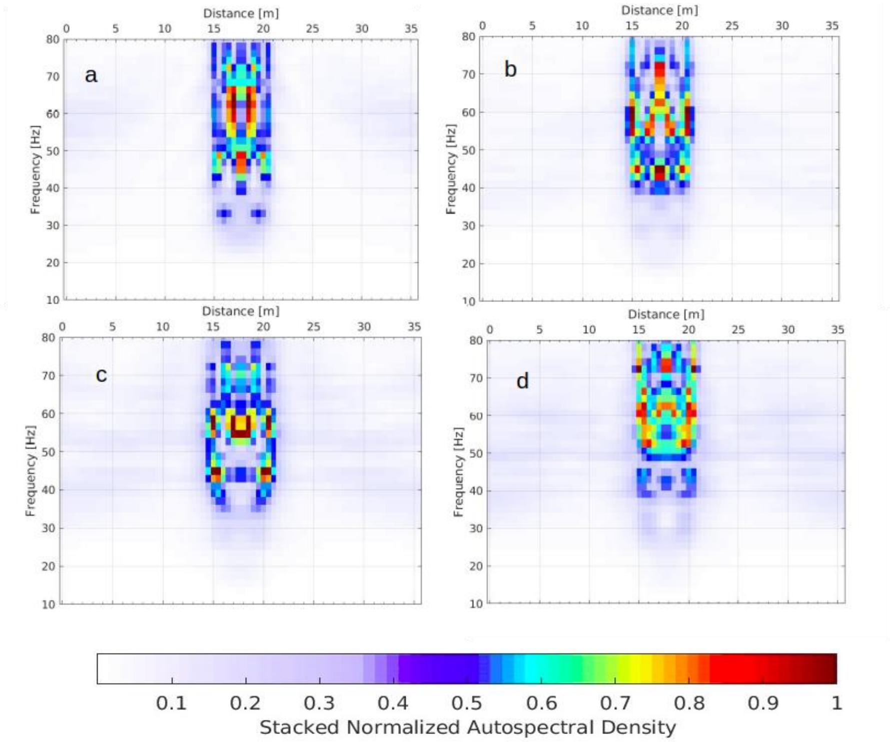

Figure 3.5 Autospectra of Box 1 for different depths a:4 m, b:6 m, c:8 m, and d:10 m computed on the simulations that adopted Ricker wavelet with central frequency equal to 30 Hz.

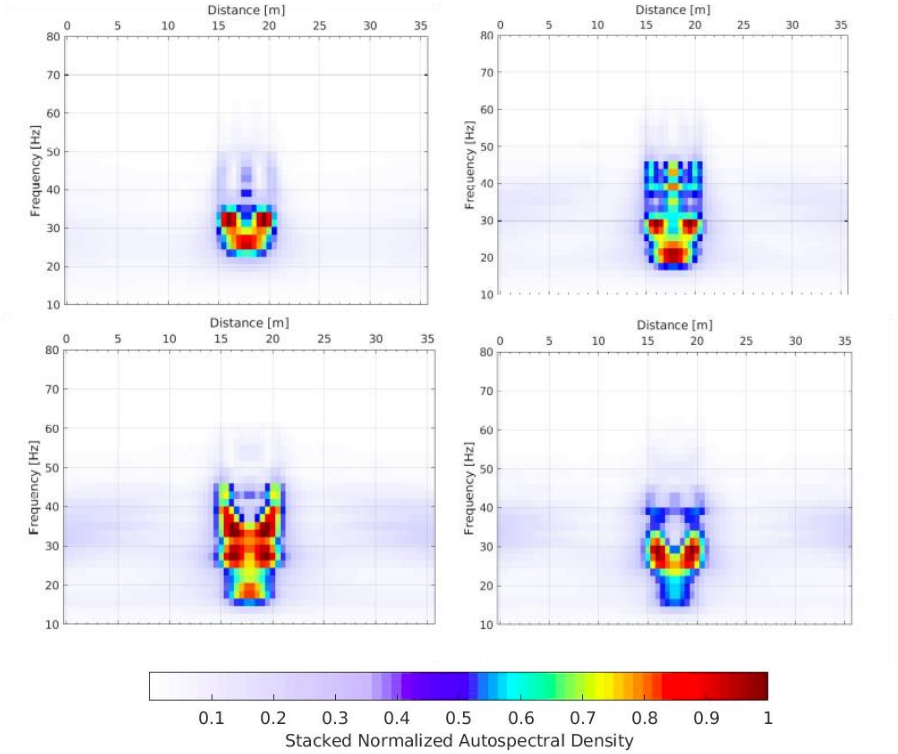

Figure 3.6 Autospectra of Box 1 for different depths a:4 m, b:6 m , c:8 m and d:10 m computed on the simulations that adopted Ricker wavelet with central frequency equal to 45 Hz.

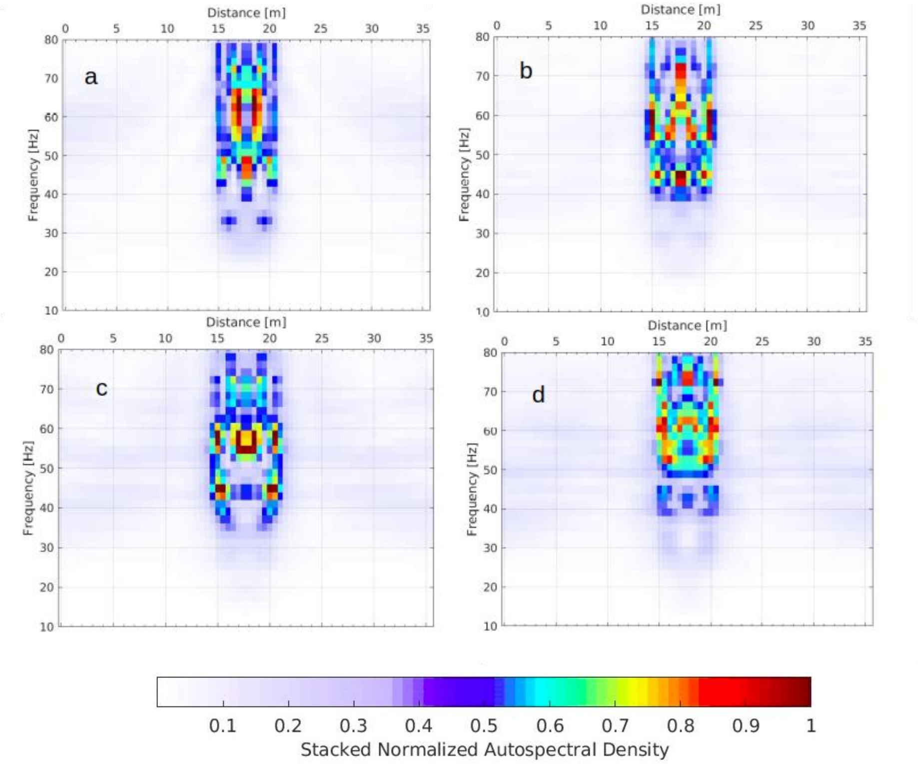

Figure 3.7 Autospectra of Box 1 for different depths a:4 m, b:6 m, c:8 m and d:10 m computed on the simulations that adopted Ricker wavelet with central frequency equal to 60 Hz.

3.3.2 Poisson's ratio effect

The second parameter whose effect on the autospectrum is investigated is Poisson's ratio. As summarized in Table 3.1, Boxes 1, 2, and 3 were modeled with Poisson's ratios of the materials equal to 0.25, 0.2, and 0.3, respectively. The autospectra of each box configuration is depicted in Figures 3.8, 3.9, and 3.10 for four different depths of the heterogeneity. Again, the selected depths are 4 m, 6 m, 8 m, and 10 m. The central frequency of the source wavelet is 45 Hz. In this case, despite minor variations in the autospectral amplitude at the different frequencies, the frequency band that is interested by the anomaly remains almost constant in the different model configurations.

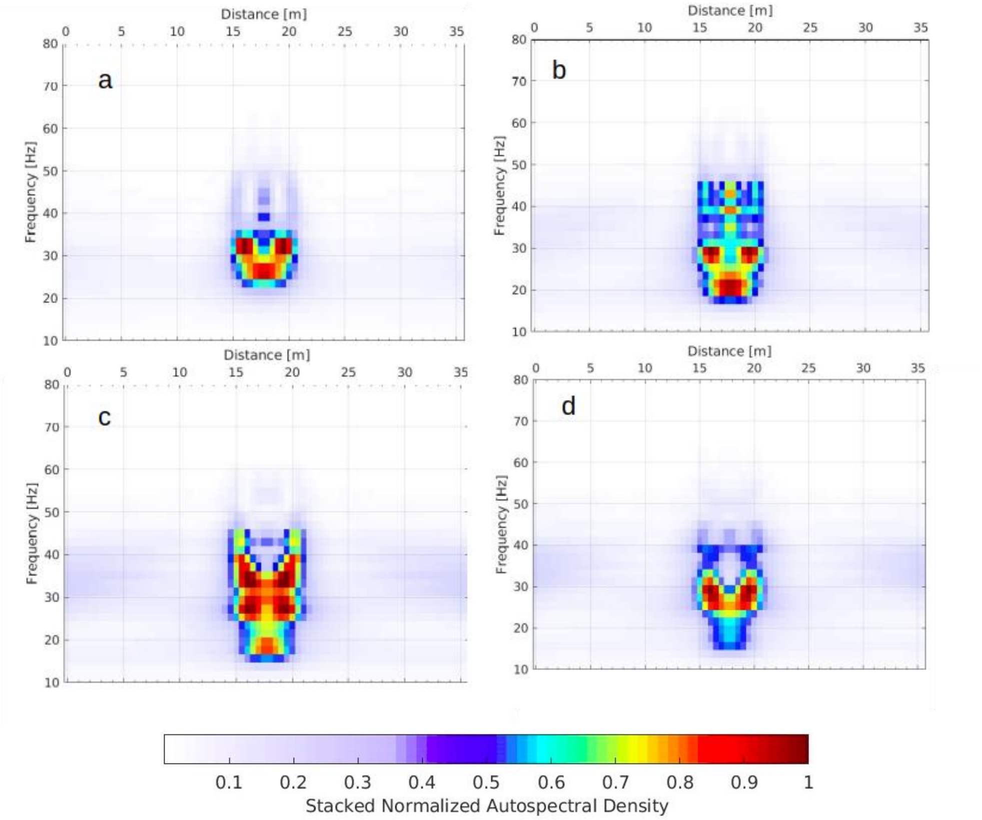

Figure 3.8. Autospectra of Box 1 for different depths a:4 m, b:6 m, c:8 m and d:10 m computed on the simulations that adopted Ricker wavelet with central frequency equal to 45 Hz.

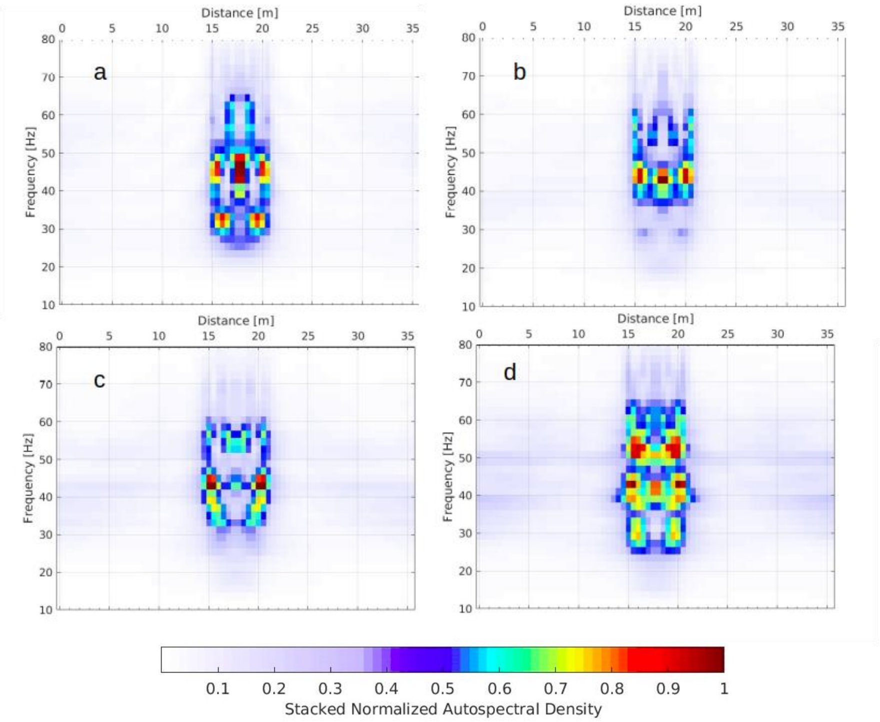

Figure 3.9. Autospectra of Box 2 for different depths a:4 m, b:6 m, c:8 m and d:10 m computed on the simulations that adopted Ricker wavelet with central frequency equal to 45 Hz.

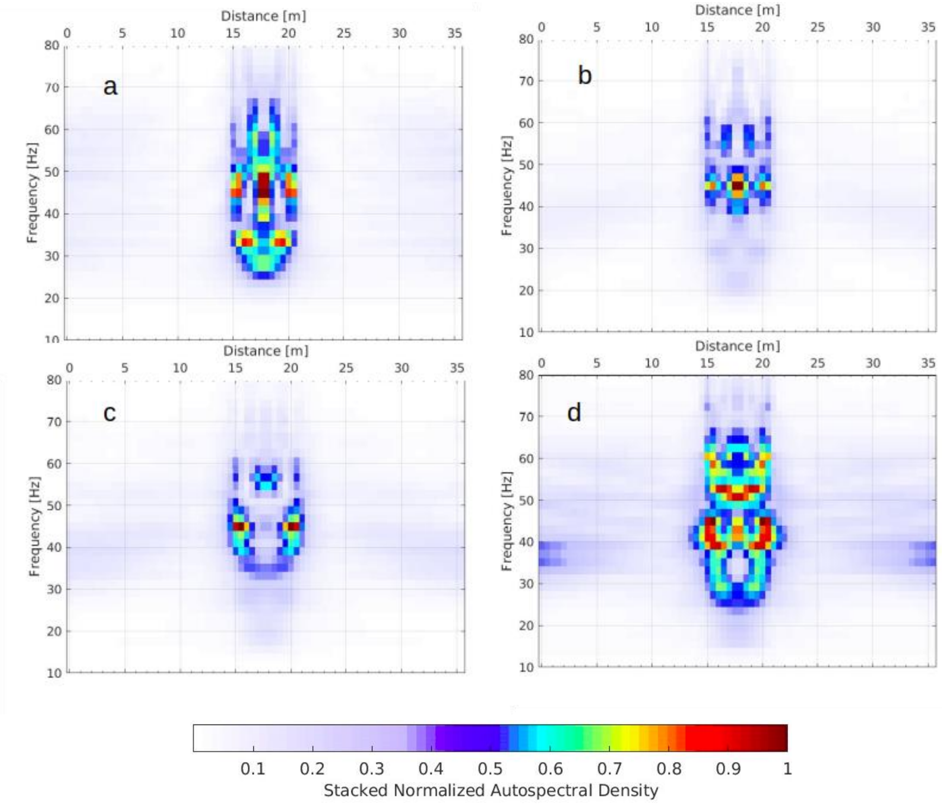

Figure 3.10. Autospectra of Box 3 for different depths a:4 m, b:6 m, c:8 m and d:10 m computed on the simulations that adopted Ricker wavelet with central frequency equal to 45 Hz.

3.3.3 Length effect

The influence of the width of the box on the autospectral results was also tested. Three different lateral lengths were defined: 4 m, 7 m, and 10 m. The boxes that are compared to each other in this section are Boxes 5, 6, and 7 in Figures 3.11, 3.12, and 3.13, respectively. The lateral variation of the models is clearly visible in these three figures, showing anomalies that are changing in width. The different length of the boxes is however also slightly affecting the frequency band interested by the anomalies, as it appears from the comparison between the same subsections of Figure 3.11 to 3.13.

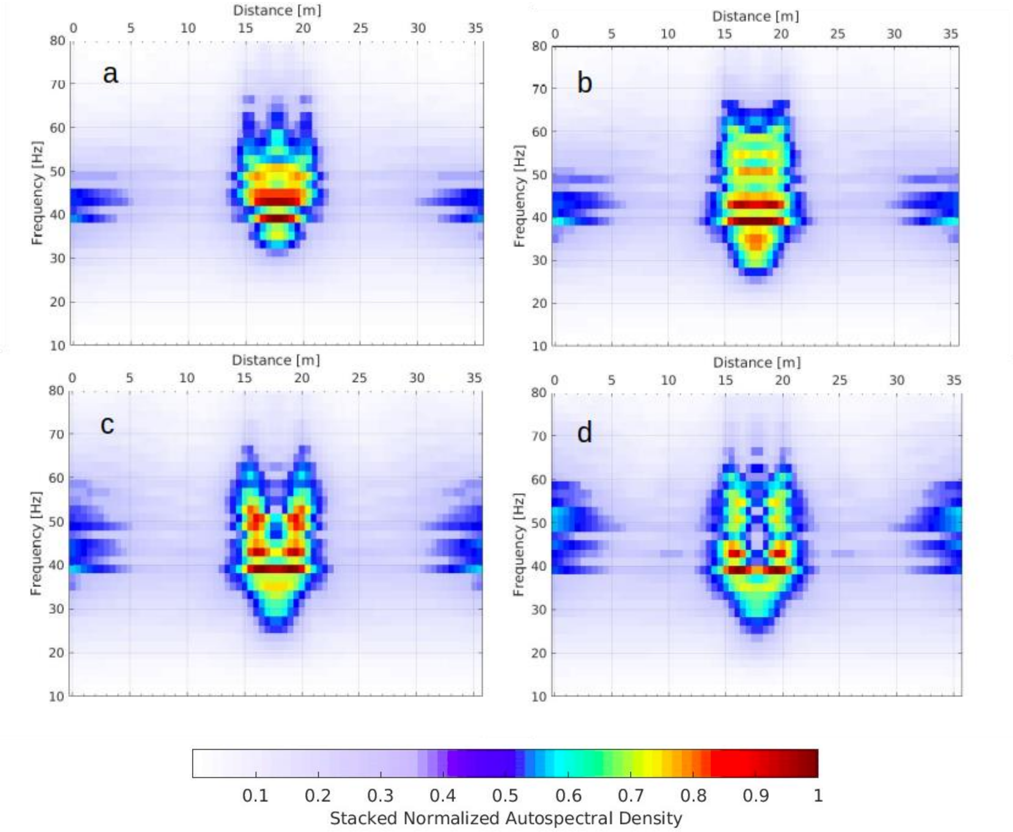

Figure 3.11. Autospectra of Box 5 for different depths a:4 m, b:6 m, c:8 m and d:10 m computed on the simulations that adopted Ricker wavelet with central frequency equal to 45 Hz and the lateral length equals to 7 m.

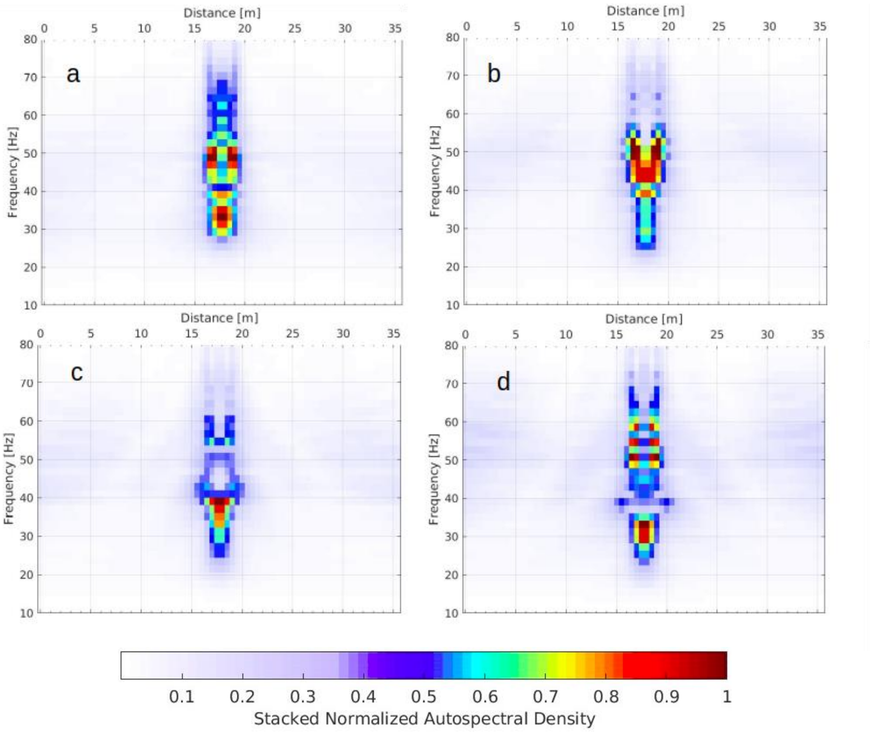

Figure 3.12. Autospectra of Box 6 for different depths a:4 m, b:6 m, c:8 m and d:10 m computed on the simulations that adopted Ricker wavelet with central frequency equal to 45 Hz and the lateral length equals to 4 m.

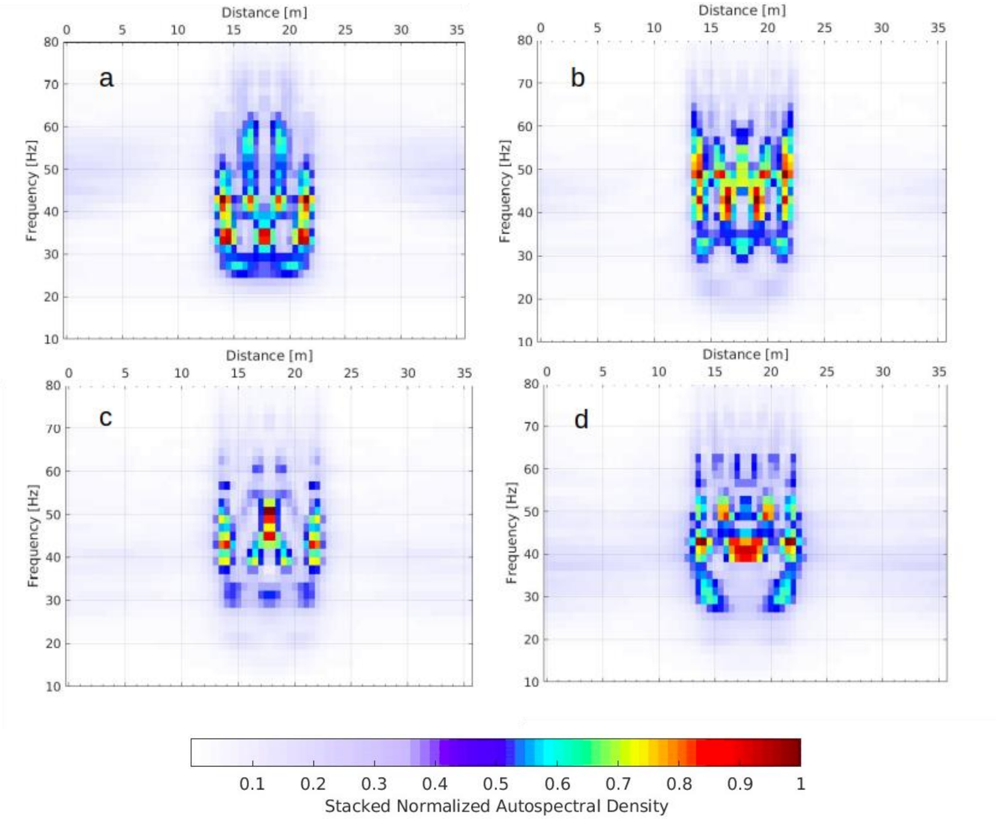

Figure 3.13. Autospectra of Box 7 for different depths a:4 m, b:6 m, c:8 m and d:10 m computed on the simulations that adopted Ricker wavelet with central frequency equal to 45 Hz and the lateral length equals to 10 m.

3.3.4 Reflection coefficient effect

The next parameter to be shown, is the reflection coefficient (RC) at the interface between Material 1 and Material 2. As it is shown in Table 3.1 the reflection coefficients differ in the Boxes 3, 4, and 5. Figures 3.14, 3.15, and 3.16 summarize the autospectra of the abovementioned boxes for different depths of the boxes. The strongest is the contrast in acoustic impedance between the materials, the most focused is the anomaly in the results. Also, in this case, the vertical frequency range affected by the anomalies is slightly varying even if comparing boxes of the same depth.

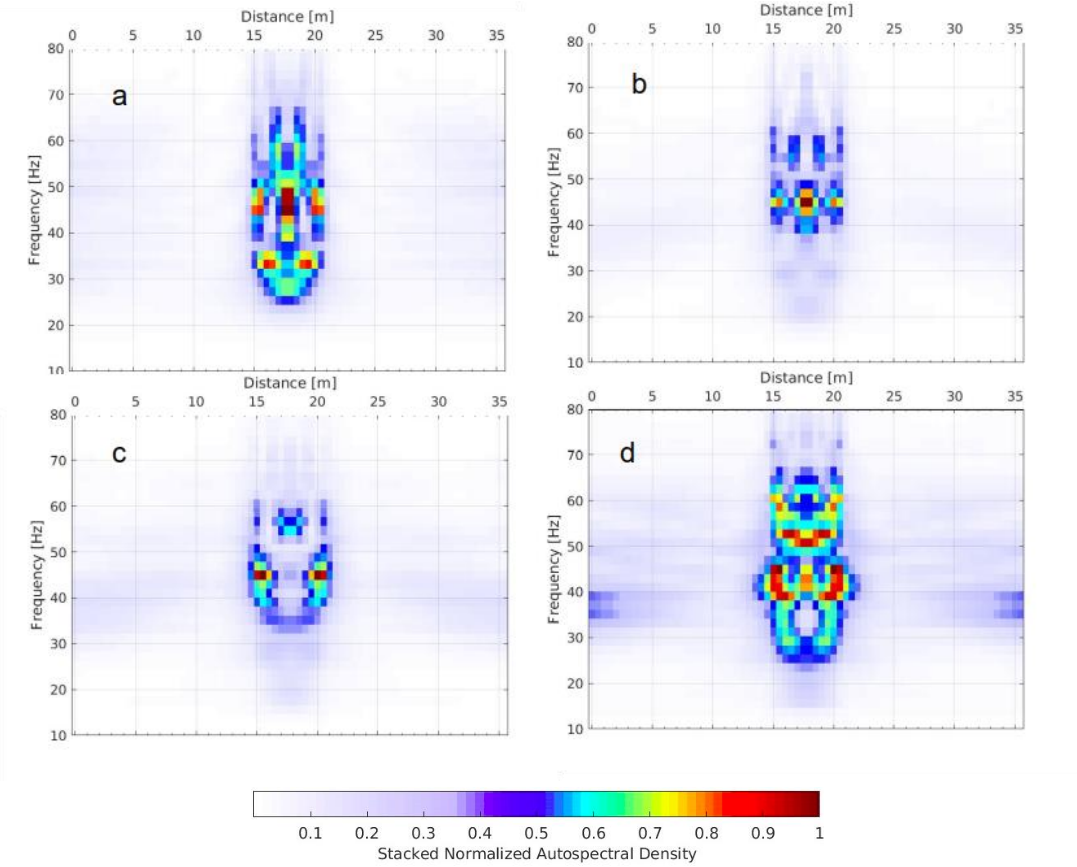

Figure 3.14. Autospectra of Box 3 for different depths a:4 m, b:6 m, c:8 m and d:10 m computed on the simulations that adopted Ricker wavelet with central frequency equal to 45 Hz and the RC is -0.48.

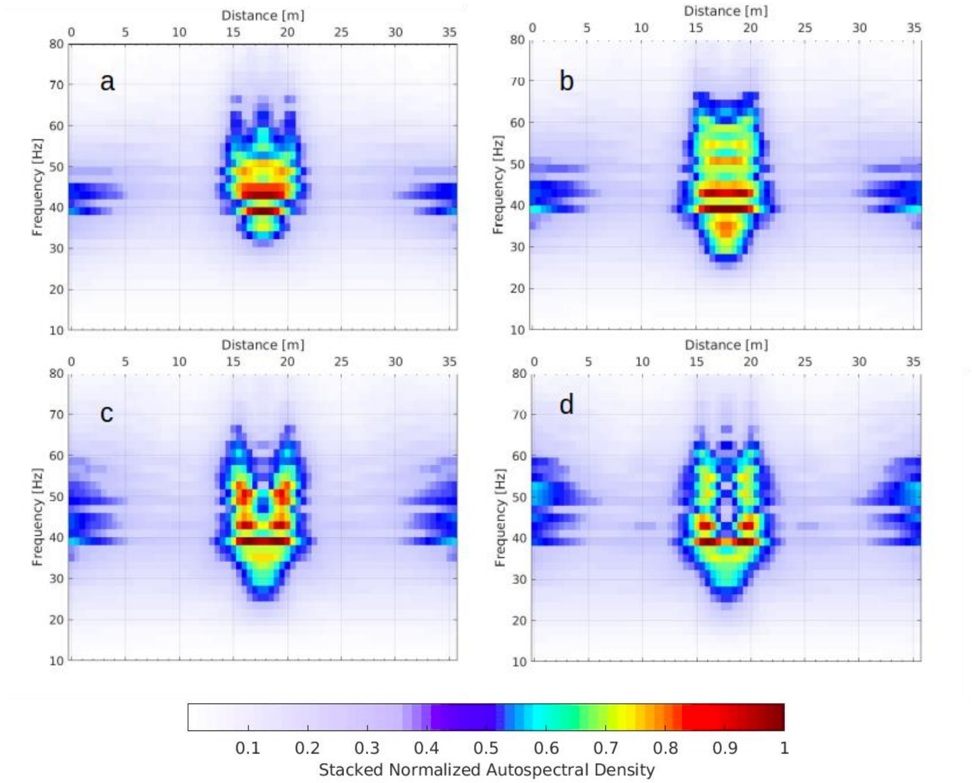

Figure 3.15. Autospectra of Box 4 for different depths a:4 m, b:6 m, c:8 m and d:10 m computed on the simulations that adopted Ricker wavelet with central frequency equal to 45 Hz and the RC is -0.31.

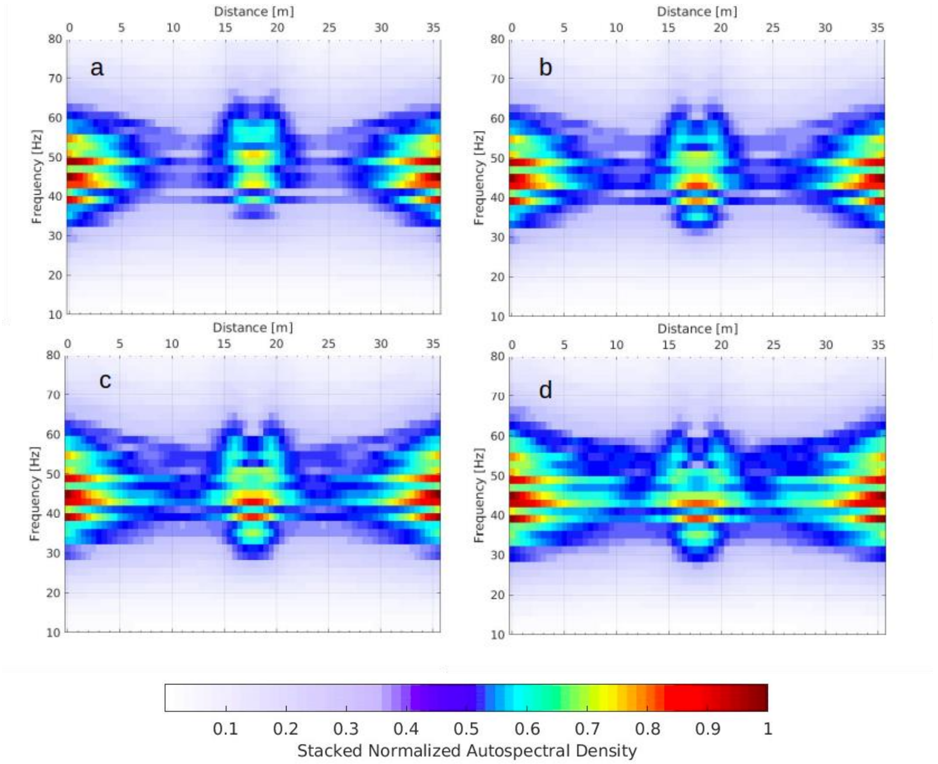

Figure 3.16. Autospectra of Box 5 for different depths a:4 m, b:6 m, c:8 m and d:10 m computed on the simulations that adopted Ricker wavelet with central frequency equal to 45 Hz and the RC is -0.17.

3.4 Deconvolved autospectrum

Deconvolution is a processing step of reflection seismic aimed at removing or attenuating the effect of the source signal on the data. Typically, deconvolution is applied before stacking. Due to deconvolution, this basic wavelet is compressed, the reverberations and multiples are attenuated, and as a result, the resolution increases. As an example, in Figure 3.17, we observe that, in addition to the points above, the ringiness of the stack section has improved by deconvolution as the process compresses the waveform at the prominent reflection. Also, in the deconvolved section, the main reflections are much more distinguishable. The role of deconvolution is not only wavelet compression, but also it removes a considerable part of the multiple energy of the section. The deconvolution or wavelet compression can be done utilizing an inverse filter as an operator of the deconvolution, as we know, by convolving an inverse filter with a wavelet, the wavelet becomes a spike. In the attribute analysis carried out in this thesis, deconvolution might consequently be tested to remove the effect of the source in the autospectral results.

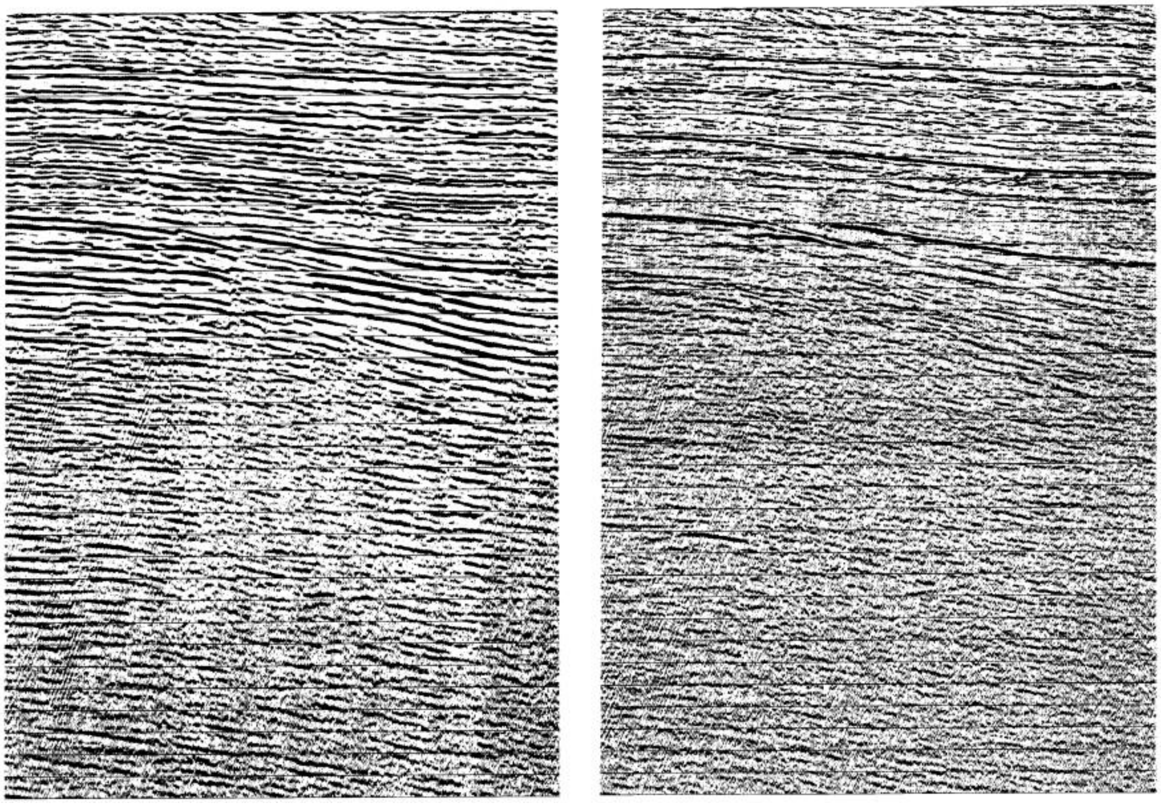

Figure 3.17 In the right section, the deconvolved stacked section is depicted, which represents much higher resolution in comparison with the left section, which shows a ringy, blurred section.

As we observe in Section 3.3.1, differences in the frequency range affected by the autospectral anomalies exist if applying a different source wavelet to the same model configuration. Since the frequency axis is of interest for the estimation of the box depth, this effect should be considered and/or removed from the data.

The deconvolved autospectra of the models as Section 3.3.1 are shown in Figures 3.18, 3.19, and 3.20. As we see in these figures the range of frequencies and the shape of the autospectra do not change if deconvolution is applied to the data. So the only parameter that made the difference between the figures in Section 3.3.1, which was the source effect, is eliminated by deconvolution.

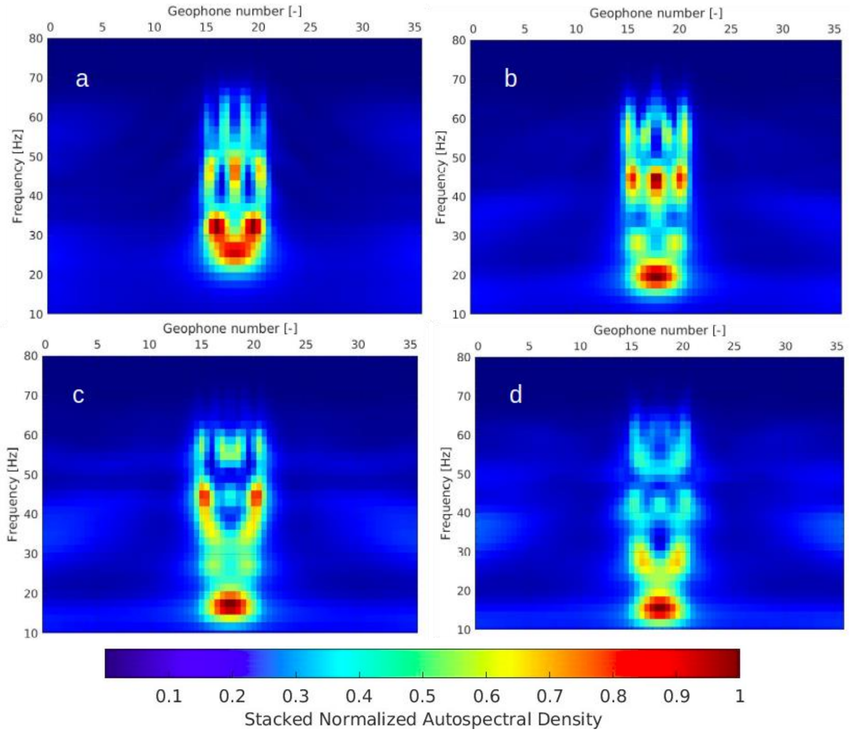

Figure 3.18. Deconvolved autospectra of Box 1 for different depths a:4 m, b:6 m, c:8 m and d:10 m computed on the simulations that adopted Ricker wavelet with central frequency equal to 30 Hz.

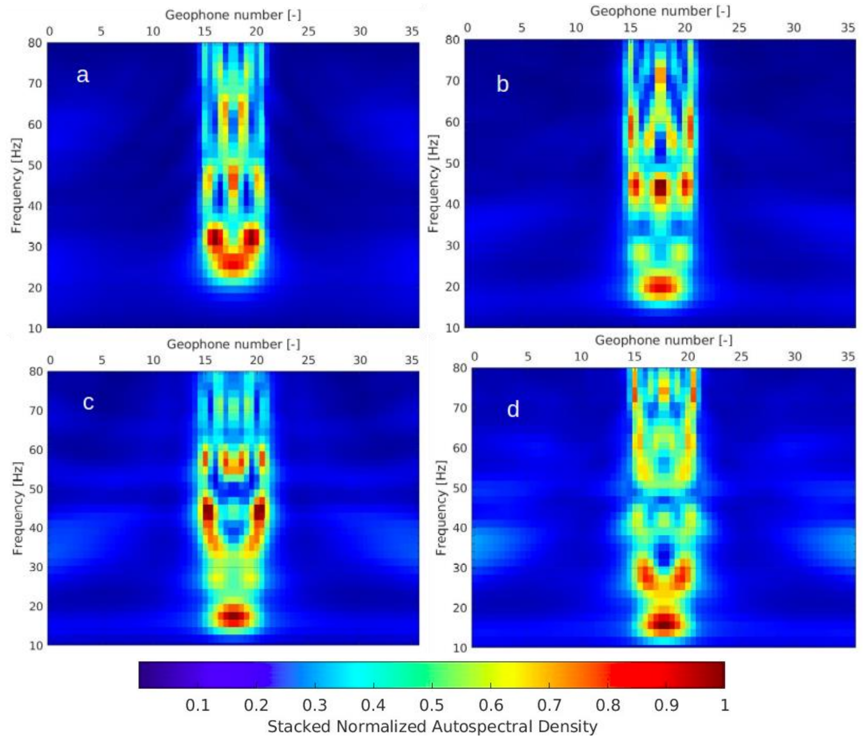

Figure 3.19. Deconvolved autospectra of Box 1 for different depths a:4 m, b:6 m, c:8 m and d:10 m computed on the simulations that adopted Ricker wavelet with central frequency equal to 45 Hz.

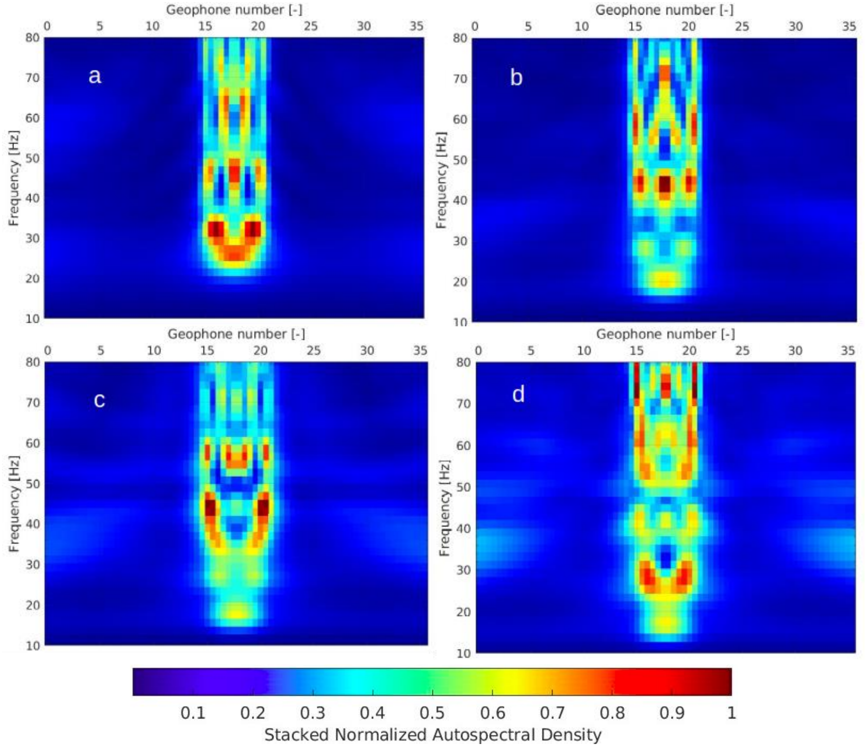

Figure 3.20. Deconvolved autospectra of Box 1 for different depths a:4 m, b:6 m, c:8 m and d:10 m computed on the simulations that adopted Ricker wavelet with central frequency equal to 60 Hz.

3.5 Frequency Selection

In order to analyze the relationship between the frequencies interested by the anomalies and the depth of the boxes, different reference frequency values were calculated on the autospectra. These frequencies were then selected as inputs for the dispersion curves of the models to retrieve the corresponding wavelength and test the wavelength-depth relationships.

To accomplish this task, the autospectral traces located inside the anomalies were summed and normalized. From the plot of the normalized autospectral sum as a function of frequency (red line in Figure 3.21), two salient frequencies were extracted: one is the frequency corresponding to the maximum autospectral density (black dot in Figure 3.21), and the other is the frequency corresponding to the bottom of the autospectral anomaly, that was fixed to 5% of the autospectral maximum value (red cross in Figure 3.21). These points are referred to as the maximum frequency and minimum frequency, respectively. On the normalized autospectral sum, also the gradient was computed (blue curve in Figure 3.21). The first maximum in the gradient was selected as an alternative way to locate the bottom interface of the anomaly (blue dot in Figure 3.21).

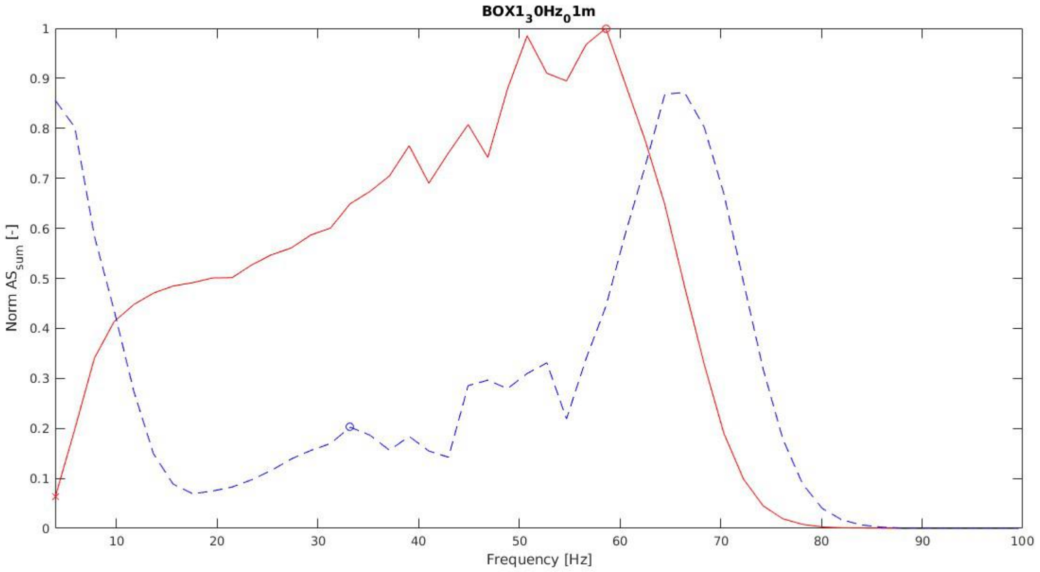

Figure 3.21 The normalized autopsectral sum (red curve) and related absolute value of its gradient (blue curve) computed on Box1, for depth of the box equal to 10 m central frequency of the wavelet equal to 30 Hz. The black dot identifies the frequency with maximum autospectral density (maximum frequency). The red cross highlights the frequency related to the bottom of the autospectral anomaly set to 5% of the maximum value (minimum frequency). The blue dot highlights the first maximum in the gradient of the autospectral sum (gradient frequency).

3.6 Estimating depth by selected frequency

After defining different approaches to frequency selection, dispersion curves can be used to estimate the wavelength interested by the anomaly at these frequencies. Figure 3.22 shows a dispersion curve computed on the box for the model Box 1 with 10 m depth and 30 Hz central frequency of the wavelet. As an explanation of the approach, in Figures 3.22, 3.23, and 3.24 we can comprehend the flow from which we can retrieve the depth estimation. First, within the dispersion curve (frequency versus velocity), we select a specific frequency, represented as f_0 (minimum frequency, maximum frequency, or gradient frequency), to extract the corresponding phase velocity V_0, as demonstrated in Figure 3.22. This velocity value is then employed as an input to the dispersion curve plotted as a function of wavelength in Figure 3.23, which yields the wavelength λ_0 as its output. By importing wavelength into the wavelength-depth relationship estimated following Socco and Comina (2017) to test its validity on the depth estimation from attribute analysis in Figure 3.24, the estimated depth from the selected frequency is also available.

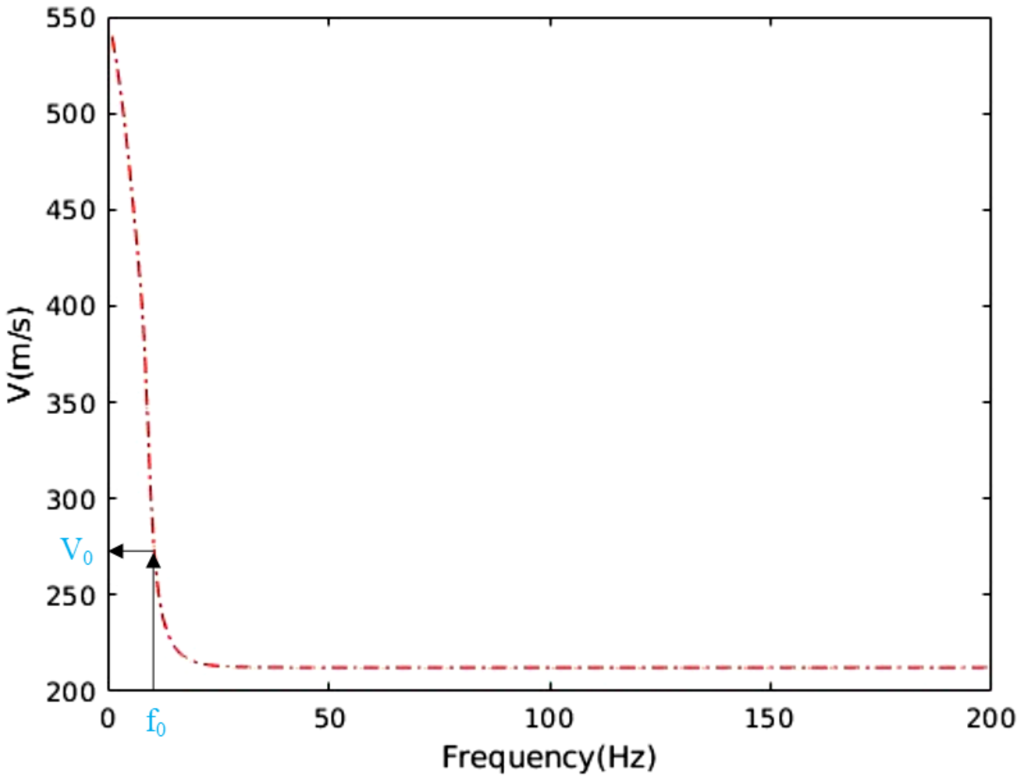

Figure 3.22 Dispersion curve (frequency – phase velocity). F_0 as an input can produce V_0. F_0 can be either minimum, maximum or gradient frequency.

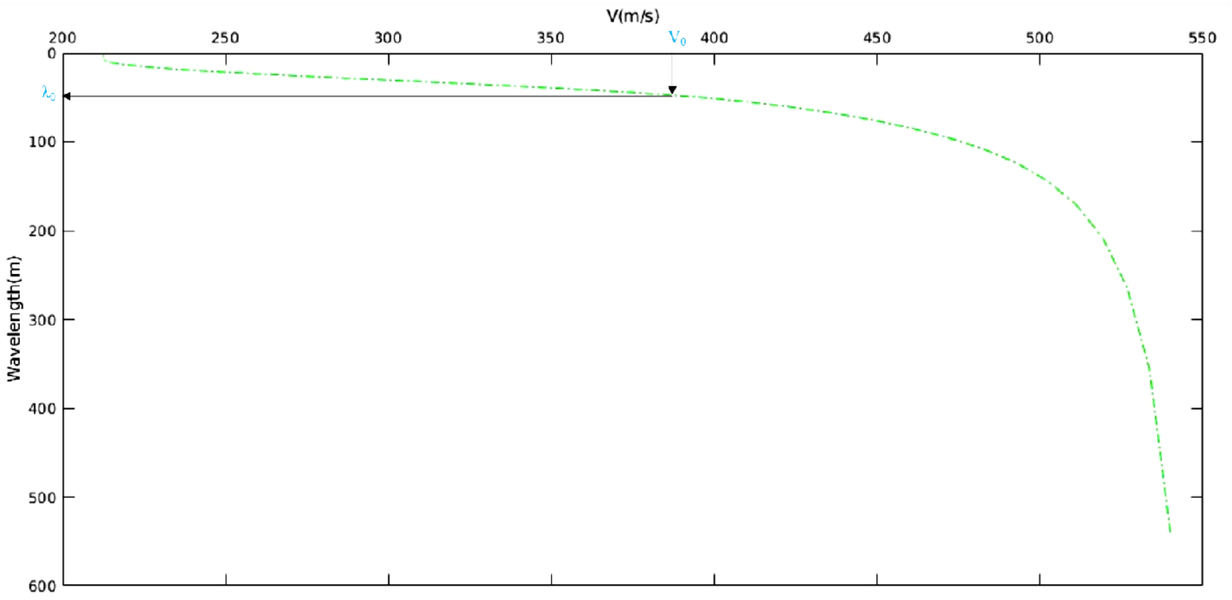

Figure 3.23 Dispersion Curve (Velocity versus wavelength). The output of Figure 3.22(V_0) is the input of this graph to retrieve wavelength.

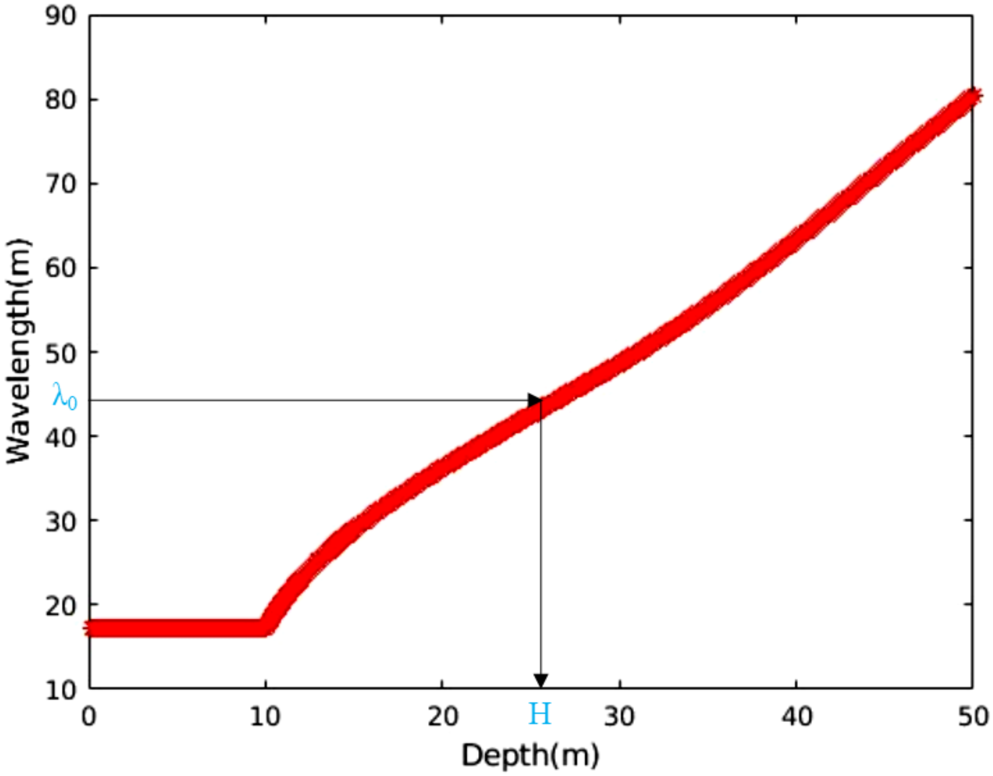

Figure 3.24 W-D relationship estimated following the approach of Socco et al. (2017). The wavelength extracted from Figure 3.24 estimates the depth.

Generally, increasing the depth of the box, the selected frequencies decrease exponentially, as shown in Figures 3.25, 3.26, and 3.27 for gradient, minimum, and maximum frequency picking respectively. This dependency illustrated in these figures confirms the primary assumption of the research and validates the depth-from-frequency approach. The curves corresponding to the deconvolved models exhibit sparsity, whereas those associated with the non-deconvolved models demonstrate closer proximity to each other. Moreover, in 1 m depth anomalies, there are high differences in frequencies, which might be due to the low thickness, which cannot be depicted correctly in the synthetic autospectra. In these figures, we can observe that the most coherent curves are those that correspond to the minimum frequency, with the only exception of very shallow anomalies (1 m) that are out of the global trend

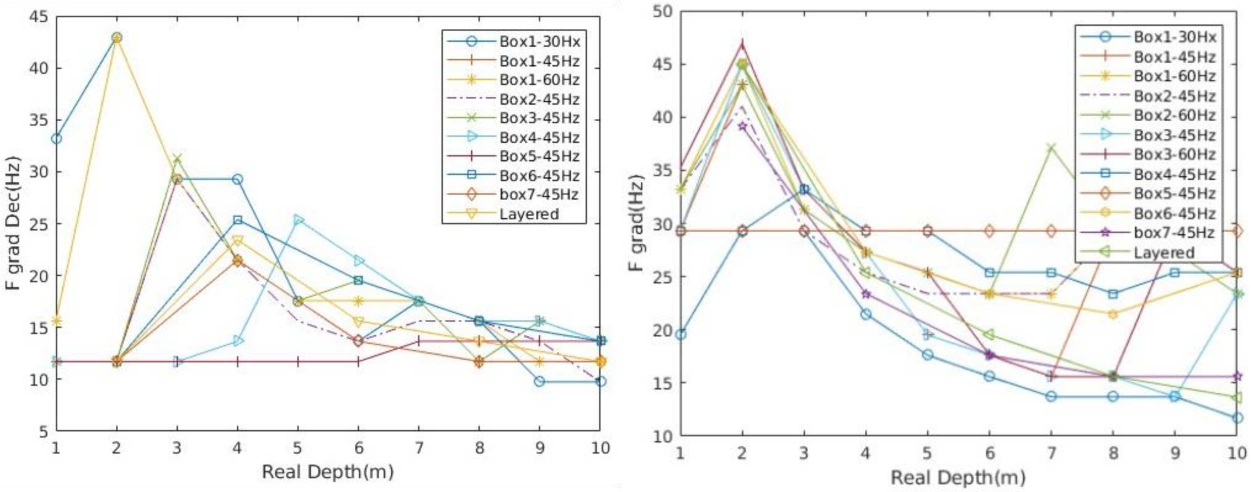

Figure 3.25 Gradient frequency versus the depth of the model. The left one is the deconvolved model and the right one is the normal model without deconvolution.

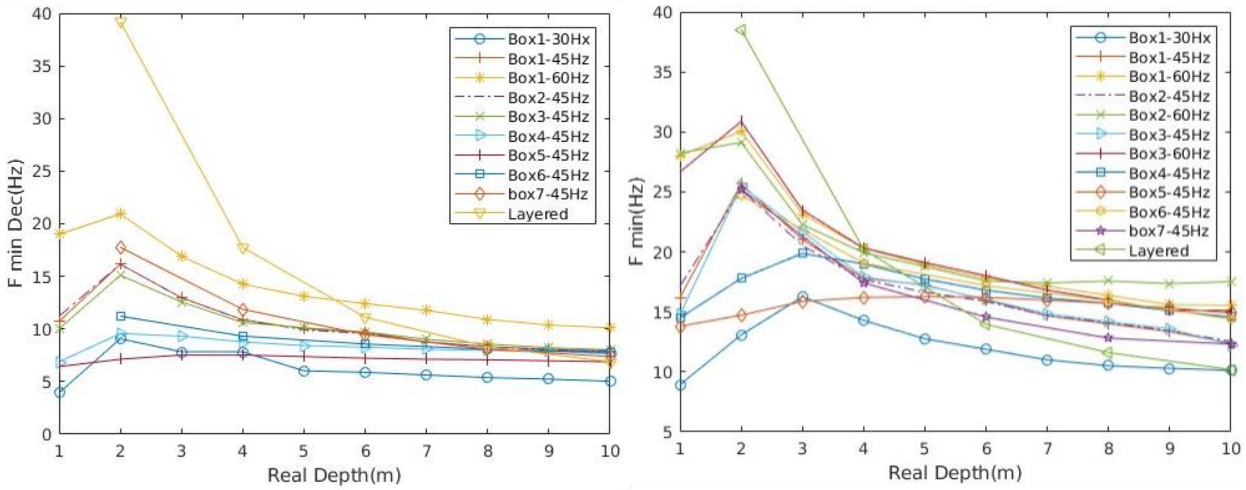

Figure 3.26 Minimum frequency versus the depth of the model. The left one is the deconvolved model and the right one is the normal model without deconvolution.

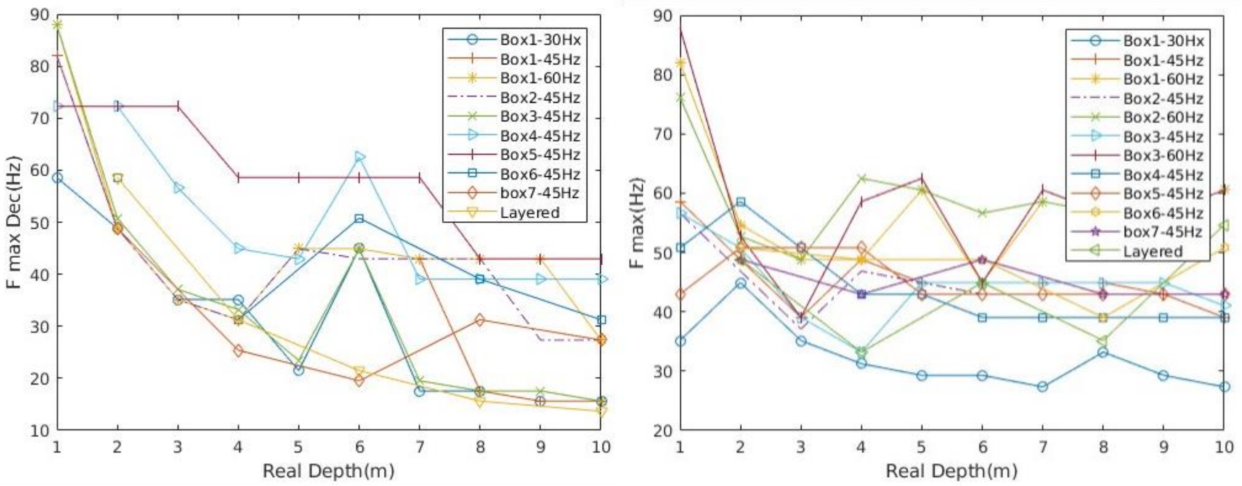

Figure 3.27 Maximum frequency versus the depth of the model. The left one is the deconvolved model and the right one is the normal model without deconvolution.

After observing the dependency of frequency on the depth of the anomaly, we can try to apply the estimation of the depth from the wavelength demonstrated by Socco et al. (2017) for the three different frequency approaches. The cross-plots of the estimated depth versus the real depth of the boxes are shown in Figures 3.28, 3.29, and 3.30 for the gradient frequency, minimum frequency, and maximum frequency respectively. In each figure, two different graphs are shown that are related to the deconvolved data and the model without deconvolution.

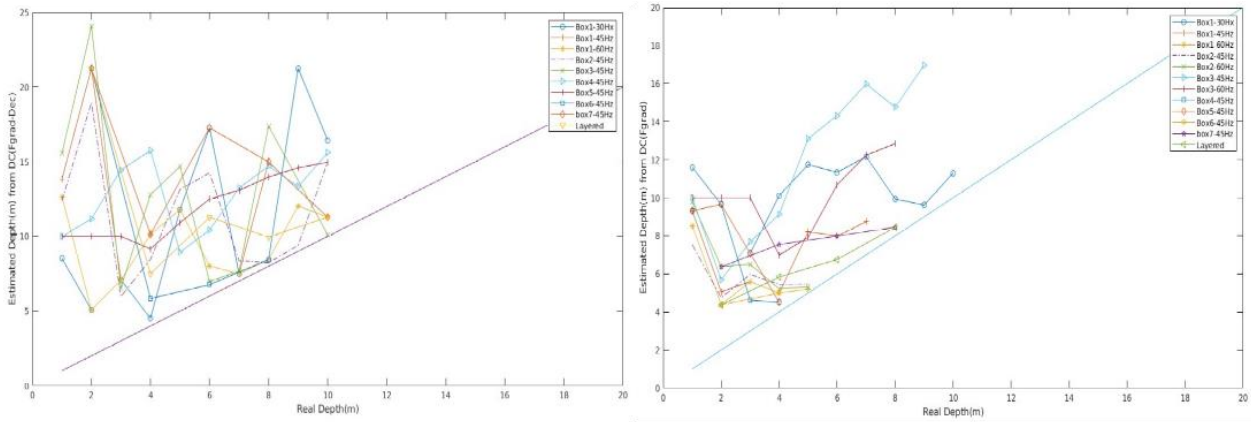

Figure 3.28 The cross-plots of the estimated depth versus real depth of the anomaly. The estimation is done by utilizing the gradient frequency. Deconvolved data (left) and raw data without deconvolution (right).

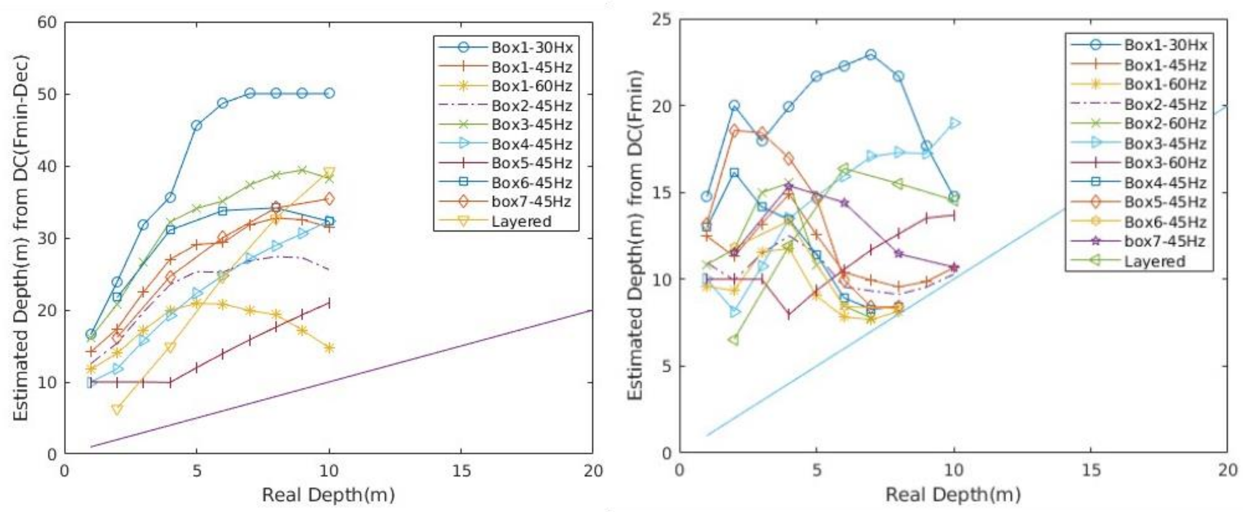

Figure 3.29 The cross-plots of the estimated depth versus real depth of the anomaly. The estimation is done by utilizing the minimum frequency. Deconvolved data (left) and raw data without deconvolution (right).

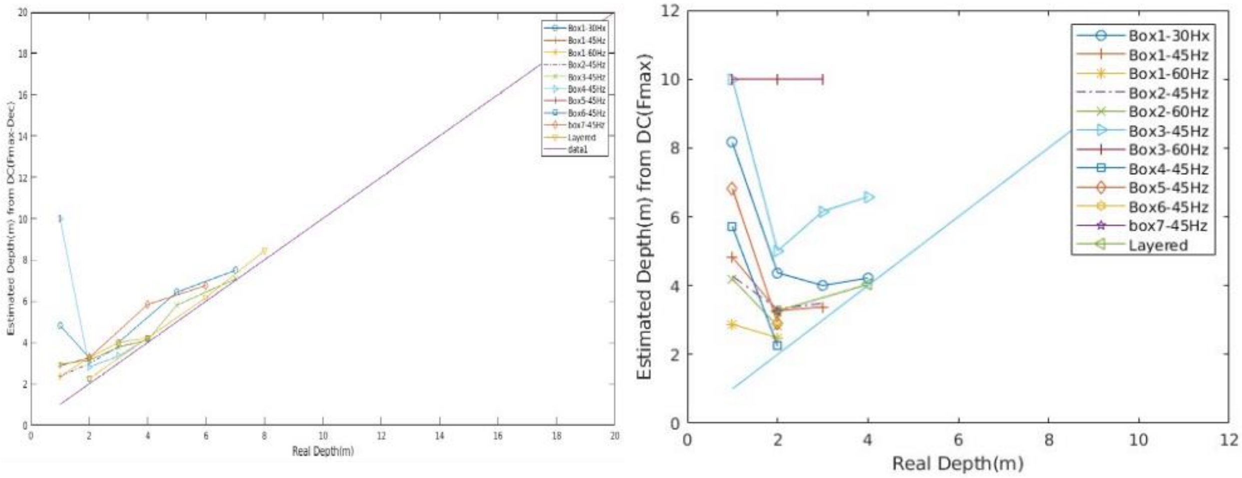

Figure 3.30 The cross-plots of the estimated depth versus real depth of the anomaly. The estimation is done by utilizing the maximum frequency. Deconvolved data (left) and raw data without deconvolution (right).

It should be noted that in Figures 3.28, 3.29, and 3.30, there are some removed points. Owing to the consistent velocity within the first layer (Material 2), the initial segment of the graph in Figure 3.24 appears entirely flat. However, as the wave transitions from Material 2 to the subsequent layer (Material 1), the wavelength undergoes variation. This transition is evident in Figure 3.24. The flatness of the initial graph segment inhibits accurate depth conversion, leading to certain null points devoid of physical significance. This phenomenon is more obvious in Figure 3.30. On the other hand, as is clear in the visual representation of the last three figures, the estimation, which is done by minimum frequency, evidently has the most coherency among others. These results illustrate that the wavelength-depth relationship is overestimating the depth. However, the maximum frequency is the one providing the closest estimation of the depth to the real values. For the linear model, it performs exceptionally well, and the depth estimation is highly robust, but in the presence of lateral heterogeneities, the application of this wavelength-depth relationship is still overestimating the depth of the boxes.

All the procedure is done in order to estimate the depth by having a relationship between the wavelength and the depth of the anomaly which is valid for all the models. Various researchers have opted to estimate depth by dividing the wavelength by an integer number (K), as depicted in Table 2.1 and Equation 2.4. Considering the proposed wavelength-depth relationship in Table 2.1, as evident in Figures 3.25, 3.26, and 3.27, the frequencies vary with the depths of the boxes. Consequently, K cannot be a constant number; it is a variable depending on the depth of the box, so there is a need to establish a new relationship. By dividing the wavelength by the depth, K is calculated. Our objective is to determine K as the value that allows us to estimate the depth with the least amount of error. Furthermore, to eliminate dependency on the depth, K is defined as follows:

$$K = \frac{\lambda}{Z} \tag{3.1}$$

Where λ is the wavelength calculated by the selected frequency and Z is the depth. Cross-plot of K versus real depth are depicted in the following figures. A regression can be applied on the new points, in the form:

$$K = a * Z^{b} \tag{3.2}$$

Where a and b are the regression coefficients. This regression can give us the desired relationship, from which the depth can achieved. By calculating R-squared value the evaluation of the goodness of the fitting relationships can be assessed. We can calculate R-squared as following:

$$R^{2} = 1 - \frac{SSR}{SST} \tag{3.3}$$

Where SSR is the sum of squared residuals, which is the sum of the squared differences between the observed values and the predicted values by the regression model, and SST is the total sum of squares, which is the sum of squared differences between the observed values and the mean of the dependent variable. In Figures, 3.31, 3.32, and 3.33, the K-Z plots of gradient frequency, minimum frequency, and maximum frequency are depicted respectively, both for the models without deconvolution and the deconvolved model.

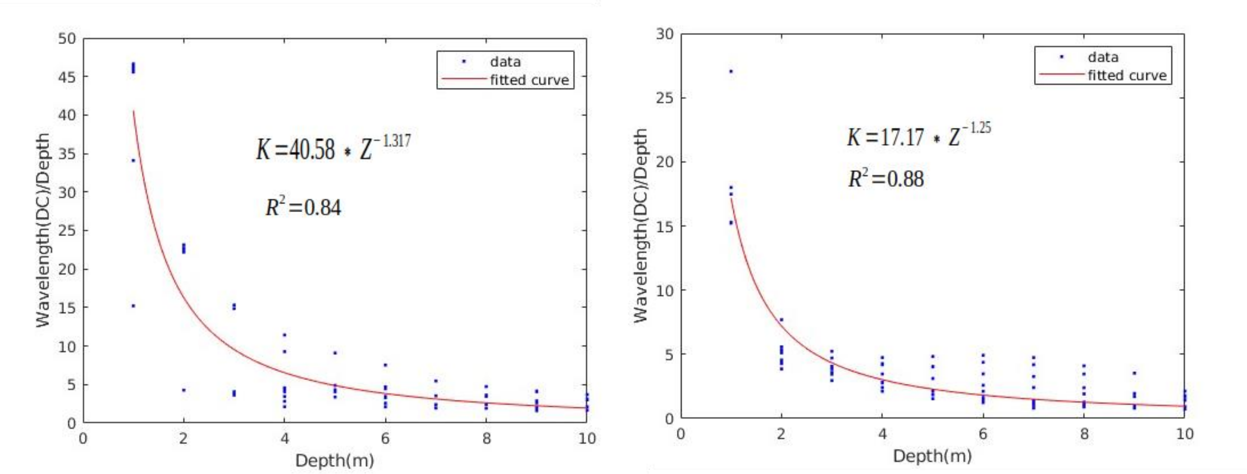

Figure 3.31 K-Z plots of the gradient frequency. The left one is related to the deconvolved model and the right one is the model without deconvolution.

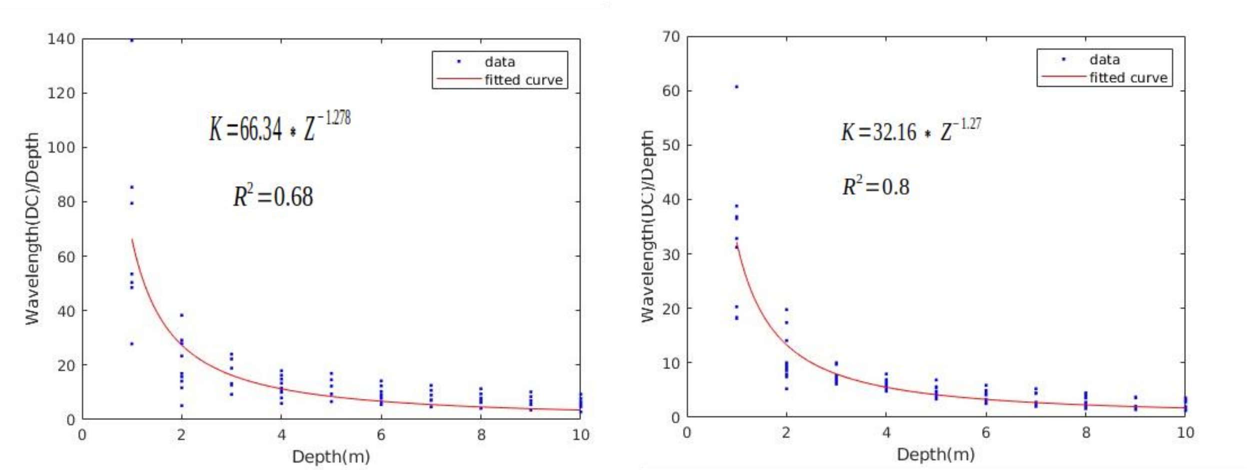

Figure 3.32 K-Z plots of the minimum frequency. The left one is related to the deconvolved model and the right one is the model without deconvolution.

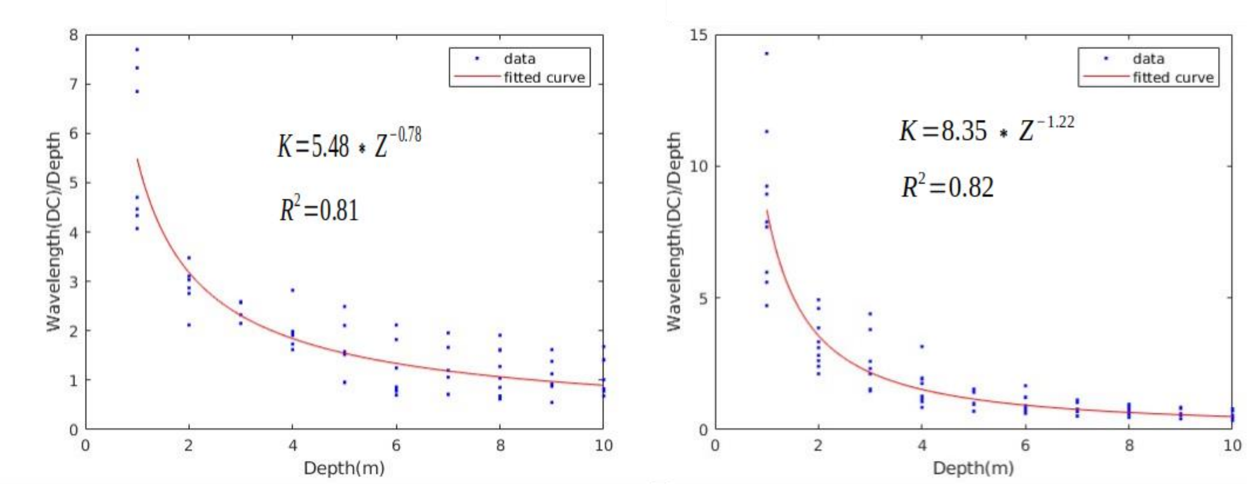

Figure 3.33 K-Z plots of the maximum frequency. The left one is related to the deconvolved model and the right one is the model without deconvolution.

As an overview of these three figures, on the one hand, the deconvolution did not help to improve the fitting of the estimation. In other words, in all three regressions, the R-squared parameter decreased due to deconvolution. On the other hand, although the most coherency can be seen in the minimum frequency, this data illustrates that the best regression belongs to the gradient frequency. Moreover, the deconvolved model of the minimum frequency in the layered shape exhibits the closest curve to the one-to-one relationship, with a correlation coefficient of 0.99 in its fitting, between the wavelength obtained from the wavelength-depth relationship and the calculated wavelength using various frequency selection methodologies. Therefore, in a layered model, wavelength can be accurately converted to depth using the wavelength-depth relationship proposed by Socco et al. (2017), but in presence of sharp lateral variations new wavelength-depth relationships must be calibrated.

Chapter 4 Conclusion

In oil and gas exploration, the Surface Wave Method (SWM) is a powerful seismic method that characterizes near-surface conditions by analyzing the geometric dispersion of surface waves. The vertical profile of shear wave velocity can be obtained by inverting the data and analyzing the dispersion characteristics derived from seismic recordings. Furthermore, it is a standard procedure to make static corrections (a method of removing the influence of weathering layers from reflection seismic data).

Significant lateral changes in the near surface can either be an additional target of investigation or a problem for the reconstruction of trustworthy subsurface models. The usefulness of SW attributes, such as autospectrum, in the identification and location of sharp lateral variations, have been proven in the literature, while their relationship with the depth and thickness of these lateral changes is still under investigation. In this thesis, we tried to investigate this relationship with a number of tests of autospectral computation on synthetic data.

The amplitude of surface waves, in our case Rayleigh waves, decreases exponentially with depth. As a consequence, the autospectrum, which is a function of wave energy and frequency, is a useful tool for studying how waves propagate in the presence of a lateral anomaly. In order to remove the effect of the source on the synthetic data, data deconvolution before autospectral computation demonstrated a valid tool to obtain autospectra not affected by the source signal. Slight variations in the frequency band affected by the autospectral anomalies were however still noted in the presence of anomalies having different lateral extension or different material properties with respect to the background.

Different autospectral frequencies were analyzed to study the dependency of the frequency and wavelength on the depth of the simulated heterogeneities. These frequencies were entered in the dispersion curve of each model to retrieve the corresponding phase velocity. The wavelength related to that phase velocity was extracted.

Wavelength-depth relationships available in the literature for depth estimation from attribute analysis and/or for the conversion of local dispersion curves in layered models were then tested on the results to investigate their applicability for the estimation of the depth of autospectral anomalies. Since none of the preexisting relationships looked suitable to describe the results, new wavelength-depth relationships were defined on the obtained numerical outcomes, to improve the depth estimation from autospectral plots.

For each salient frequency identified in the autospectra, a fitting relationship was proposed and an R-squared evaluation was done. The best fitting results were retrieved for the gradient frequency approach (R^2=0.88) on raw data without deconvolution. However, the minimum frequency and the maximum frequency approaches resulted in additional good fitting relationships with R^2 higher than 0.8. All these approaches might be therefore reliable for depth estimation, but further tests are needed to analyze the validity of the defined relationships on real data.

References

Aung, A. M. W., and E. C. Leong, 2015, Application of weighted average velocity (WAVe) method to determine V S;30: Soils and Foundations, 55,548–558, doi: 10.1016/j.sandf.2015.04.007.

Bergamo, P., and L. V. Socco, 2014, Detection of sharp later discontinuities through the analysis of surface-wave propagation: Geophysics, 79, no. 4,EN77–EN90, doi: 10.1190/geo2012-0031.1.

Bièvre, G., D. Jongmans, T. Winiarski, and V. Zumbo, 2012, Application of geophysical measurements for assessing the role of fissures in water infiltration within a clay landslide (Trieves area, French Alps): Hydrological Processes, 26, 2128–2142, doi: 10.1002/hyp.v26.14.

Boiero, D., and L. V. Socco, 2011, The meaning of surface wave dispersion curves in weakly laterally varying structures: Near Surface Geophysics, 9, 561–570, doi: 10.3997/18730604.2011042.

Brown, L. T., J. G. Diehl, and R. L. Nigbor, 2000, A simplified procedure to measure average shear-wave velocity to a depth of 30 meters (V S;30): Presented at the 12th World Conference on Earthquake Engineering.

Carpentier, S. T. A., A. G. Green, R. Langridge, F. Hurter, A. Kaiser, H. Horstmeyer, and M. Finnemore, 2012, Seismic imaging of the Alpine Fault near Inchbonnie, New Zealand: Journal of Geophysical Research: Solid Earth, 118, 416–431, doi: 10.1029/2012JB009344.

Colombero, C., C. Comina, and L.V. Socco, 2020, Imaging near-surface sharp lateral variations with surface-wave methods — Part 1: Detection and location: GEOPHYSICS, VOL. 84, NO. 6; P. EN93–EN111, 27 FIGS., 6 TABLES. DOI:10.1190/GEO2019-0149.1

Colombero, C., C. Comina, G. Umili, and S. Vinciguerra, 2016, Multiscale geophysical characterization of an unstable rock mass: Tectonophysics, 675, 275–289, doi: 10.1016/j. tecto.2016.02.045.

Colombero, C., L. Baillet, C. Comina, D. Jongmans, and S. Vinciguerra, 2017, Characterization of the 3-D fracture setting of an unstable rock mass: From surface and seismic investigations to numerical modeling: JGR Solid Earth, 122, 1–21, doi: 10.1002/2017jb014111.

Comina, C., S. Foti, D. Boiero, and L. V. Socco, 2011, Reliability of V S;30 evaluation from surface waves tests: Journal of Geotechnical and Geoenvironmental Engineering, 137, 579–586, doi: 10.1061/(ASCE)GT.1943-5606.0000452.

Evanse, and Dragoset, 1997, A Handbook for Seismic Data Acquisition in Exploration number 7, Gischig, V. S., E. Eberhardt, J. R. Moore, and O. Hungr, 2015, On the seismic response of deep seated rock slope instabilities — Insights from numerical modeling: Engineering Geology, 193, 1–18, doi: 10.1016/j.enggeo.2015.04.003.

Galvis, I. S., Villa, Y., Durate, C., Sierra, D., and Agudelo, W., 2017, Seismic attribute selection and clustering to detect and classify surface waves in multicomponent seismic data by using k-means algorithm, SEG, doi.org/10.1190/tle360300239.1.

Grandjean G. and Bitri A. 2006. 2M-SASW: Multifold multichannel seismic inversion of local dispersion of Rayleigh waves in laterally heterogeneous subsurfaces: Application to the Super-Sauze earthflow, France. Near Surface Geophysics 4, 367–375.

Haney, M., and R. Miller, 2013, Introduction to this special section: Non reflection seismic and inversion of surface waves and guided waves: The Leading Edge, 32, 610–611, doi: 10.1190/tle32060610.1.

Hévin, G., O. Abraham, H. A. Pedersen, and M. Campillo, 1998, Characterization of surface cracks with Rayleigh waves: A numerical model: NDT and E International, 31, 289–297, doi: 10.1016/S0963-8695(98)80013-3.

Hyslop, C., and R. R. Stewart, 2015, Imaging lateral heterogeneity using reflected surface waves: Geophysics, 80, no. 3, EN69–EN82, doi: 10.1190/geo2014-0066.1.

Ikeda, T., and T. Tsuji, 2016, Surface wave attenuation in the shallow subsurface from multichannel-multishot seismic data: A new approach for detecting fractures and lithological discontinuities: Earth, Planets and Space, 68, 1–14, doi: 10.1186/s40623-016-0487-0.

Kennett B.L.N. and Yoshizawa K. 2002. A reappraisal of regional surface wave tomography. Geophysical Journal International 150, 37–44.

Lin C. and Lin C. 2007. Effect of lateral heterogeneity on surface wave testing: Numerical simulations and a countermeasure. Soil Dynamics and Earthquake Engineering 27, 541–552.

Nasseri-Moghaddam, A., G. Cascante, and J. Hutchinson, 2005, A new quantitative procedure to determine the location and embedment depth of a void using surface waves: Journal of Environmental and Engineering Geophysics, 10, 51–64, doi: 10.2113/JEEG10.1.51.

Pierre-Yves, 1985, The two-dimensional resonance of sediment-filled valleys: Bulletin of the Seismological Society of America, Vol. 75, No. 2, pp. 519-541, DOI: 10.1785/BSSA0750020519

Shtivelman, V., 2003, Application of shallow seismic methods to engineering, environmental and groundwater investigations: Bollettino di Geofisica Teorica ed Applicata Vol. 44, n. 3-4.

Socco, L.V., and C._Strobbia, 2004, Surface-wave method for near surface characterization: a Tutorial: Near Surface Geophysics, 2(4):165-185,DOI:10.3997/1873-0604.2004015.

Socco, L. V., and C. Comina, 2017, Time-average velocity estimation through surface-wave analysis: Part 2: P-wave velocity: Geophysics, 82, this issue, doi: 10.1190/geo2016-0368.1.

Socco, L. V., G. Mabyalaht, and C. Comina, 2015, Robust static estimation from surface wave data: 85th Annual International Meeting, SEG, Expanded Abstracts, 5222–5227.

Strobbia, C., A. Laake, P. Vermeer, and A. Glushchenko, 2011, Surface waves: Use them then lose them. Surface-wave analysis, inversion and attenuation in land reflection seismic surveying: Near Surface Geophysics, 9, 503–513, doi: 10.3997/1873-0604.2011022.

Strobbia, C., and S. Foti, 2006, Multi-offset phase analysis of surface wave data (MOPA): Journal of Applied Geophysics, 59, 300–313, doi: 10.1016/j.jappgeo.2005.10.009.

Telford, W. M., Sheriff, R. E., & Geldart, L. P. (1990). Applied Geophysics. [2nd Edition]. [The Press Syndicate of the University of Cambridge].147-149.

Yilmaz, O., Z. 1987, Seismic data analysis, Processing, inversion and interpretation of Seismic Data, Vol 1, Electronic edition, 388.

Zerwer, A., M. A. Polak, and J. C. Santamarina, 2005, Detection of surface breaking cracks in concrete members using Rayleigh waves: Journal of Environmental and Engineering Geophysics, 10, 295–306, doi: 10.2113/JEEG10.3.295.